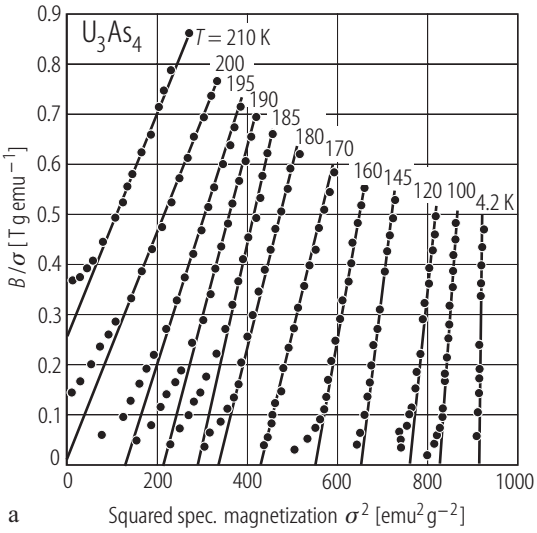

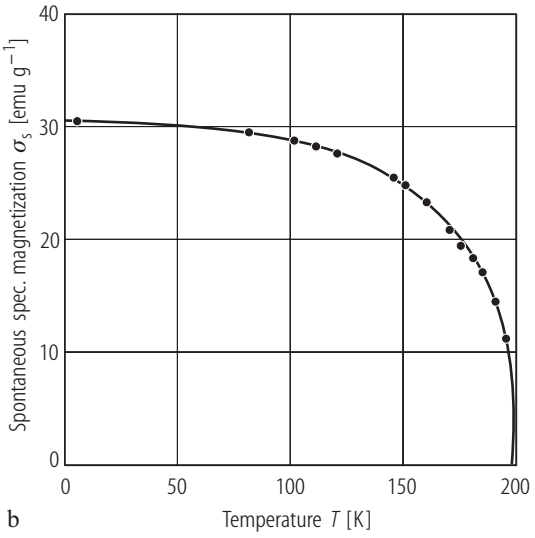

Fig. 131. U_3As_4, sc. **(a)** Magnetization isotherms in the form of the Arrott's plot B/σ vs. σ^2 [81TM]. The measurement temperatures are specified in the figure, the magneic field was applied along the [111] axis. The solid lines are linear extrapolations to $B/\sigma = 0$. **(b)** Spontaneous magnetization, σ_s, along the [111] easy axis vs. temperature, T, data derived by the Arrott's method [81BRTH]. The solid curve serves as a guide for the eye. The spontaneous magnetic moment is 1.83 μ_B.

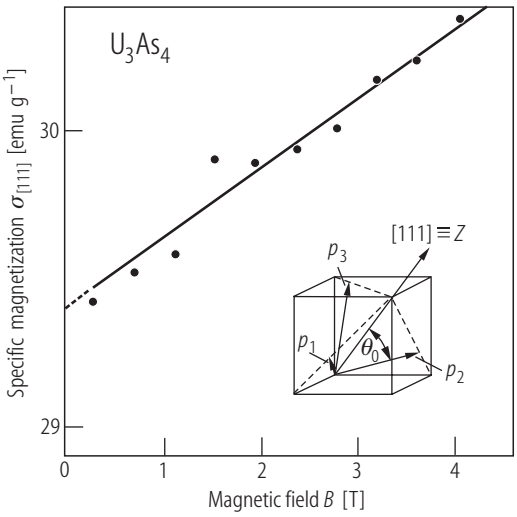

Fig. 132. U_3As_4, sc. Specific magnetization, σ, vs. magnetic field, B, up to 4 T taken at 4.2 K with $B \parallel [111]$ [77NRS]. The high-field susceptibility, χ_{hf}, determined from the slope of $\sigma(B)$ amounts to $2.4 \cdot 10^{-5}$ emu/g. Extrapolation of $\sigma(B)$ to $B = 0$ yields a magnetic moment of 1.78 μ_B/U atom, in agreement with that given in [81BRTH]. Inset: the suggested magnetic structure.

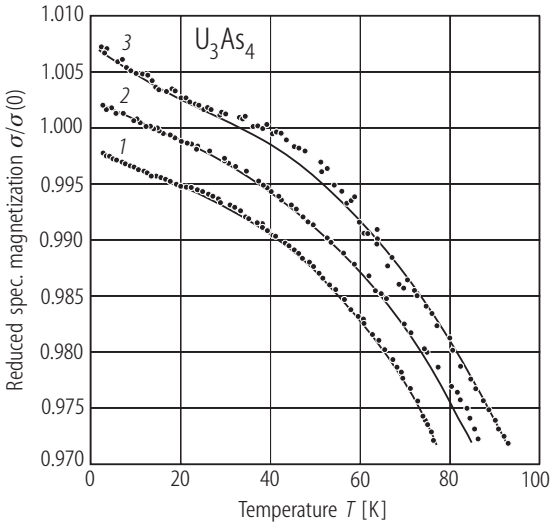

Fig. 133. U_3As_4, sc. Reduced magnetization, $\sigma/\sigma(0)$, vs. temperature, T, below 100 K, taken with magnetic field applied along the [111] axis [82MKTS]. Curve *1*) B = 1.1 T; *2*) 3.2 T; *3*) 8.5 T. Note unusual steps in the magnetization near 40 K. The solid lines are the least-square fits of the experimental data to the expression: $\sigma(T,B)/\sigma(0,0) = a(B)T^{3/4} + b(B)T^2 \exp(-\frac{\Delta(B)}{T})$. For explanation and the fitting parameters see the original paper.

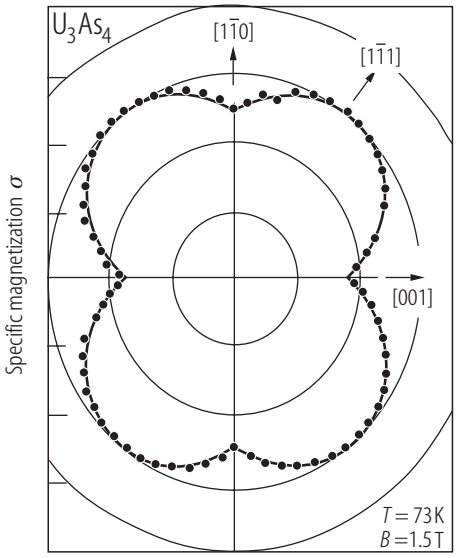

Fig. 134. U_3As_4, sc. Angular variation of the magnetization, σ, measured within the (110) plane in a field of 1.5 T at T = 73 K [69B]. The uranium ordered magnetic moment along the easy direction [111] amounts to 1.82 μ_B.

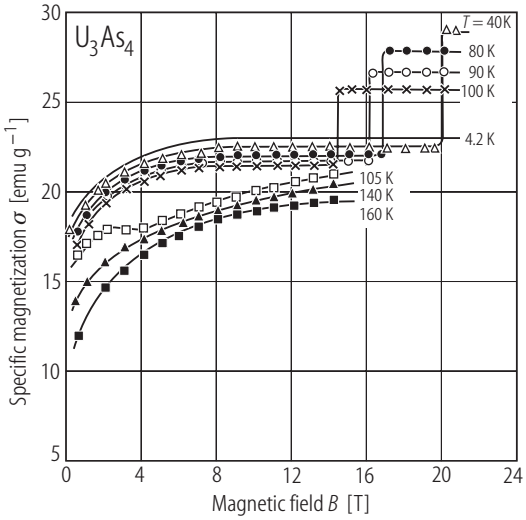

Fig. 135. U_3As_4, sc. Specific magnetization, σ, along the [100] axis vs. magnetic field, B, up to 21 T, measured at various temperatures as indicated [81TSNM]. The solid lines serve as a guide for the eye. Note that between 40 and 100 K there occur magnetization jumps at the critical fields B_c between 20.5 and 14 T. At T = 105 K, the $\sigma(T)$ curve exhibits only a plateau over a magnetic field range of about 2 T. Note also that the high-field magnetization above B_c does not reach the values found for B || [111] (compare Fig. 132) being in agreement with the theoretical prediction from [80K1].

For Fig. 136 see next page

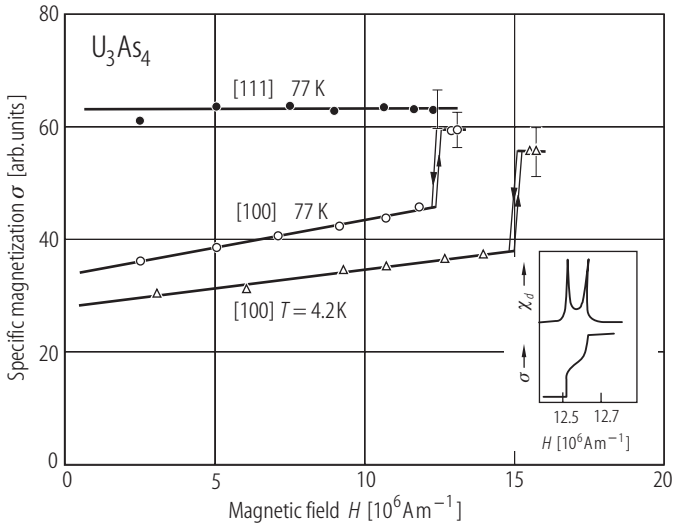

Fig. 137. U_3As_4, sc. Specific magnetization, σ, vs. pulsed magnetic field, H, up to 16 MA/m taken at T = 77 K (circles) and T = 4.2 K (triangles) with H || [111] (full symbols) and H || [100] (open symbols) [76NS]. Note a sudden jump in the magnetization measured along the [100] direction with strongly temperature dependent magnitude and field position. Inset: $\sigma(H)$ and differential susceptibility, $\chi_d(H)$, measured at 77 K with H || [100] in the vicinity of the critical field, H_c. Note two sharp peaks in $\chi_d(H)$ corresponding to the onset and to the end of the transition. The width of the transition is 0.12 and 0.16 MA/m at 4.2 and 77 K, respectively. The hysteresis in H_c amounts to 0.16 MA/m at 4.2 K.

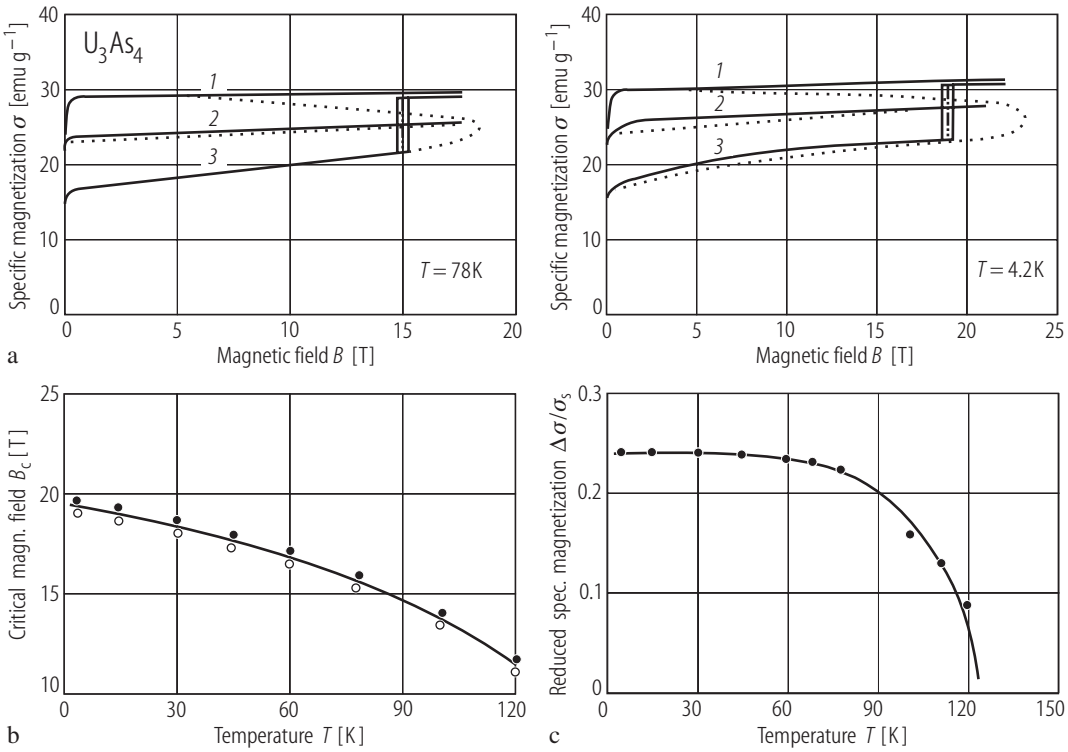

Fig. 136. U_3As_4, sc. **(a)** Specific magnetization, σ, vs. pulsed magnetic field, B, measured at T = 78 K (left-hand side panel) and T = 4.2 K (right-hand side panel) with (curve *1*) B || [111], *2*) B || [110] and *3*) B || [100] [80BLOY]. Note a jump in the magnetization measured along the [100] direction occurring at a critical field B_c = 19.1 and 15.3 T at 4.2 and 78 K, respectively. The dotted lines are theoretical $\sigma(B)$ curves calculated on the basis of the anisotropy constants presented in Fig. 144. **(b)** Critical field, B_c, of the magnetization jump vs. temperature, T [80BLOY]. The open and full circles correspond to the B_c value obtained with increasing and decreasing field, respectively. The solid line is a guide to the eye. See also Fig. 139a. **(c)** Relative magnitude of the magnetization jump, $\Delta\sigma/\sigma_s$, vs. temperature, T, where σ_s is the saturation magnetization measured above the magnetization discontinuity [80BLOY]. The solid line serves as a guide to the eye. Note that $\Delta\sigma/\sigma_s$ hardly changes at low temperatures and starts to decrease rapidly only above 80 K. Compare the results presented in Fig. 139b.

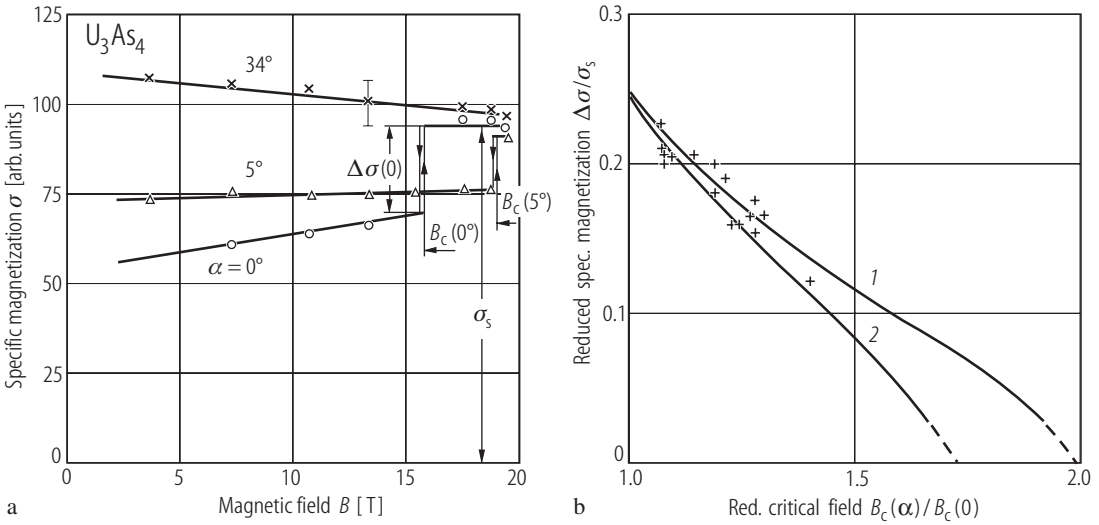

Fig. 138. U_3As_4, sc. **(a)** Specific magnetization, σ (arb. units), vs. magnetic field, B, up to 20 T taken at T = 77 K with B making an angle $\alpha = 0°$ (circles), 5° (triangles) and 34° (crosses) with the [001] direction in the (110) plane [77KN]. σ_s is the saturation magnetization measured above the magnetization discontinuity. Note that both the magnitude of the magnetization jump, $\Delta\sigma$, and the value of the critical field B_c are functions of α. **(b)** Reduced magnetization discontinuity, $\Delta\sigma/\sigma_s$, vs. reduced value of the critical transition field, $B_c(\alpha)/B_c(0)$, as derived from the experimental data (crosses) shown in panel **(a)** [77KN]. The solid lines are the calculated curves. For curve 1) $K_1 = -2.67 \cdot 10^5$ J/m^3, $K_2 = -3.45 \cdot 10^7$ J/m^3, $K_3 = K_4 = 0$ and for curve 2) $K_1 = -16.1 \cdot 10^5$ J/m^3, $K_2 = K_3 = 0$, $K_4 = -6.83 \cdot 10^7$ J/m^3, where K_i denote the anisotropy constants in the extended expression for the anisotropy energy (for details see the original paper). Note that both theoretical curves are in agreement with the experiment, and in both cases the higher-order anisotropy terms (K_2, K_4) are considerably larger than the constant K_1.

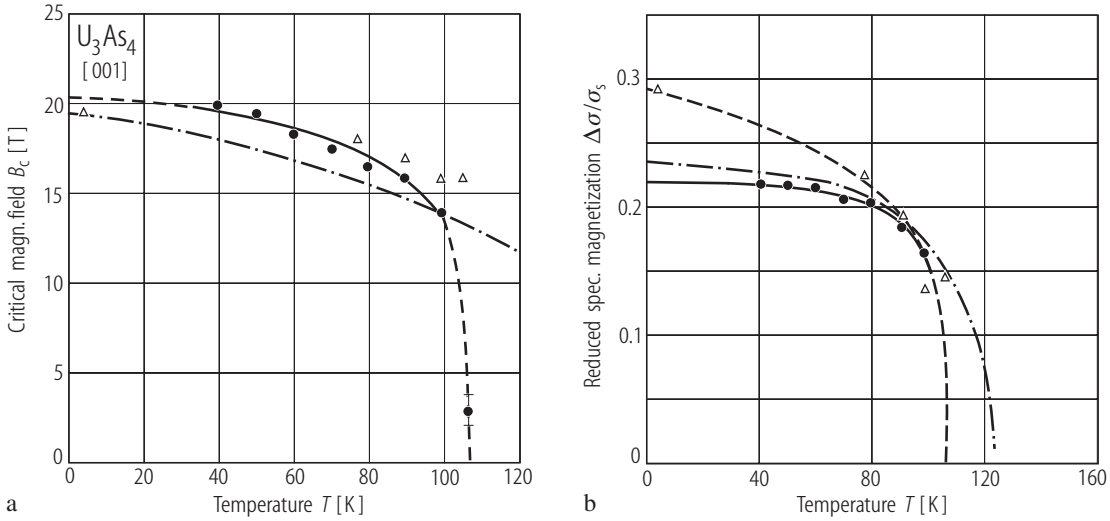

Fig. 139. U_3As_4, sc. **(a)** Critical field for the spin reorientation transition, B_c, vs. temperature, T [81TSNM]. Full circles: the data from Fig. 135; open triangles: the data from [77NS]. Note that B_c suddenly drops to zero near 105 K. For comparison the dash-pointed curve represents the results obtained in pulsed magnetic fields by [80BLOY] with no rapid decrease in B_c at least up to 130 K (see Fig. 136b). **(b)** Relative magnetization jumps, $\Delta\sigma/\sigma_s$, vs. temperature T [81TSNM]. Full circles and solid curve represent the data from Fig. 135, open triangles and dashed curve are the results obtained by [77NS], while dash-pointed curve corresponds to the data measured in pulsed magnetic fields by [80BLOY]. Note an apparent disagreement between the results of different authors.

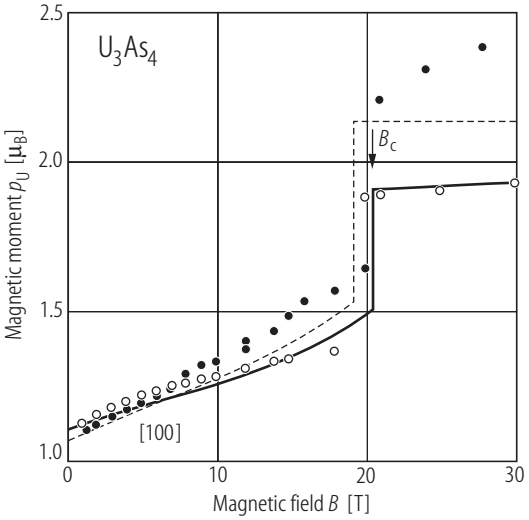

Fig. 140. U_3As_4, sc. Magnetic moment per U atom, p_U, along the [100] axis vs. pseudostatic magnetic field, B, up to 30 T, measured at T = 5K [95BWHF]. Open and filled circles correspond to two different single crystals. The solid and dashed lines are calculated $\sigma(B)$ curves for two non-collinear ferromagnetic structures C_1 and C_2, respectively, predicted in [89MHFV] (see Fig. 189). It is suggested that the two crystals measured correspond to these two different phases, which differ in the tilting angle of the uranium magnetic moments from the [111] axis. At a critical field B_c there occurs a spin reorientation transition considered as a transition to a collinear ferrimagnetic L phase, which was also predicted in [89MHFV] (compare this statement with Figs. 36 and 40a).

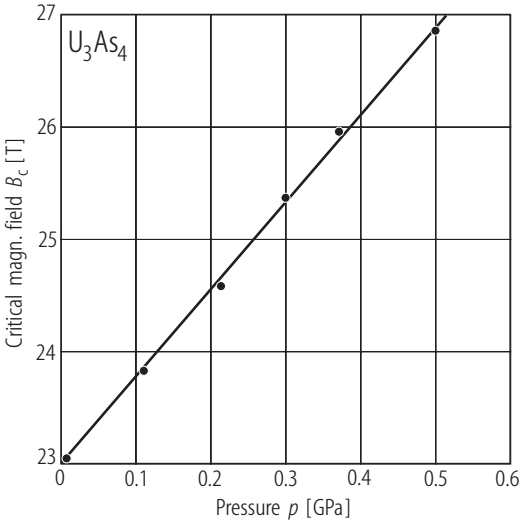

Fig. 141. U_3As_4, sc. Critical field for the spin reorientation transition, B_c, vs. pressure, p, up to 0.5 GPa, measured at T = 5 K with $B \parallel$ [100] [95BWHF]. Note a straight-line behaviour of $B_c(p)$ with the slope dB_c/dp = 7.6 T/GPa. The difference in B_c measured at normal pressure outside (20.5 T) and inside (23 T) the pressure vessel is due to a small misalignment (< 2°) between the [100] axis and the magnetic field direction in the latter case (compare Fig. 140).

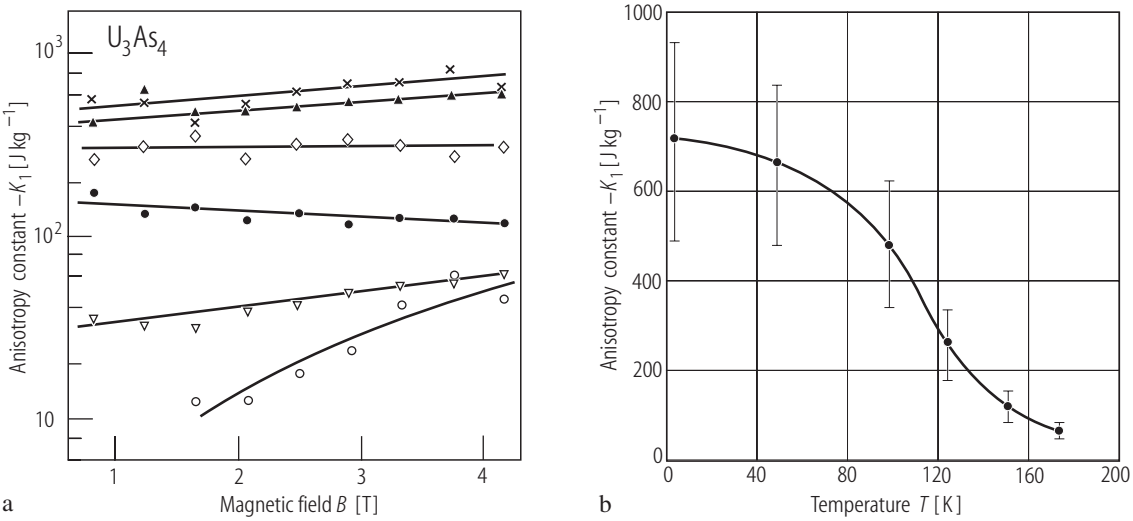

Fig. 142. U_3As_4, sc. **(a)** Anisotropy constant, K_1, vs. magnetic field, B, calculated from experimental magnetization curves measured in the temperature range 4.2…200 K along the [111] and [100] directions [79Z]. Crosses: T = 4.2 K; full triangles up: T = 100 K; open diamonds: T = 125 K; full circles: T = 150 K; open triangles down: T = 175 K; open circles: T = 200 K. Note that the character of the curves depends on temperature, particularly in the vicinity of T_C = 198 K. **(b)** Anisotropy constant, K_1, vs. temperature, T, derived from the data presented in panel **(a)** by extrapolation $1/B \rightarrow 0$ [79Z].

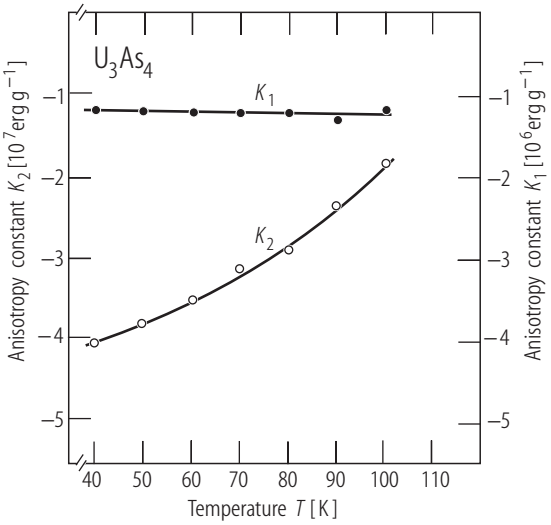

Fig. 143. U_3As_4. Cubic anisotropy coefficients, K_1 (full circles; right-hand side scale) and K_2 (open circles; left-hand side scale), vs. temperature, T, in the range 40…100 K [81TSNM]. K_1 and K_2 were derived from the temperature dependence of B_c (see Fig. 139a). Note that the two constants differ by almost one order of magnitude. For comparison see the results given in Fig. 144.

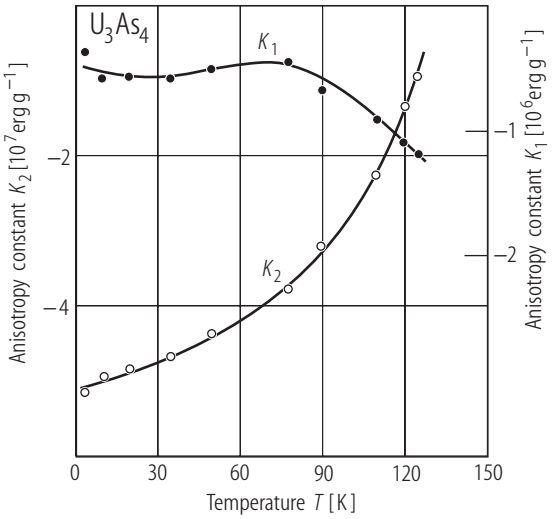

Fig. 144. U_3As_4. Magnetic anisotropy constants, K_1 (full circles) and K_2 (open circles), vs. temperature, T, in the range 4.2…130 K [80BLOY]. The anisotropy was calculated from the experimental data of $\Delta\sigma(T)/\sigma_s$ presented in Fig. 136c. Note that both anisotropy constants are negative and $|K_1| << |K_2|$. The absolute values $|K_1|$ and $|K_2|$ are lower and higher, respectively, than those displayed in Fig. 143.

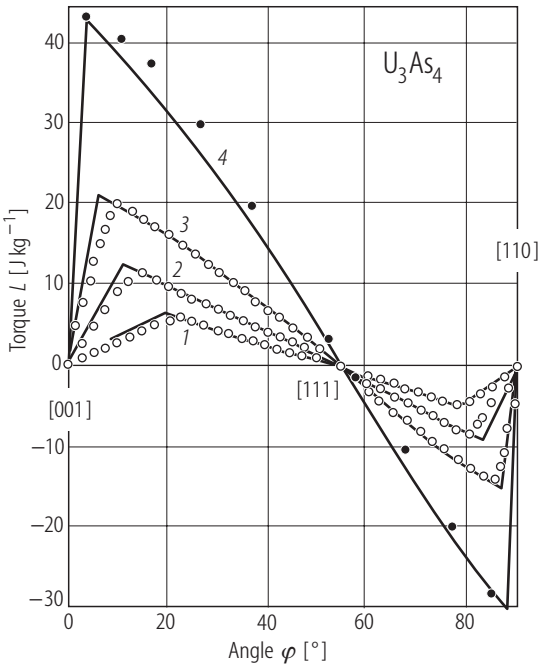

Fig. 145. U_3As_4, sc. Torque curves $L(\varphi)$ measured in various fields applied in the (110) plane of a spherical sample at T = 60 K (open symbols) and 78 K (full circles) [81Z1]. Curve *1*: 0.37 T, *2*: 0.61 T; *3*: 0.965 T; *4*: 1.9 T. The T = 78 K data are taken from [73BHDL]. The solid lines are theoretical curves. Note a good agreement between the experimental and calculated results, confirming that the easy magnetization axis in U_3As_4 is the [111] direction.

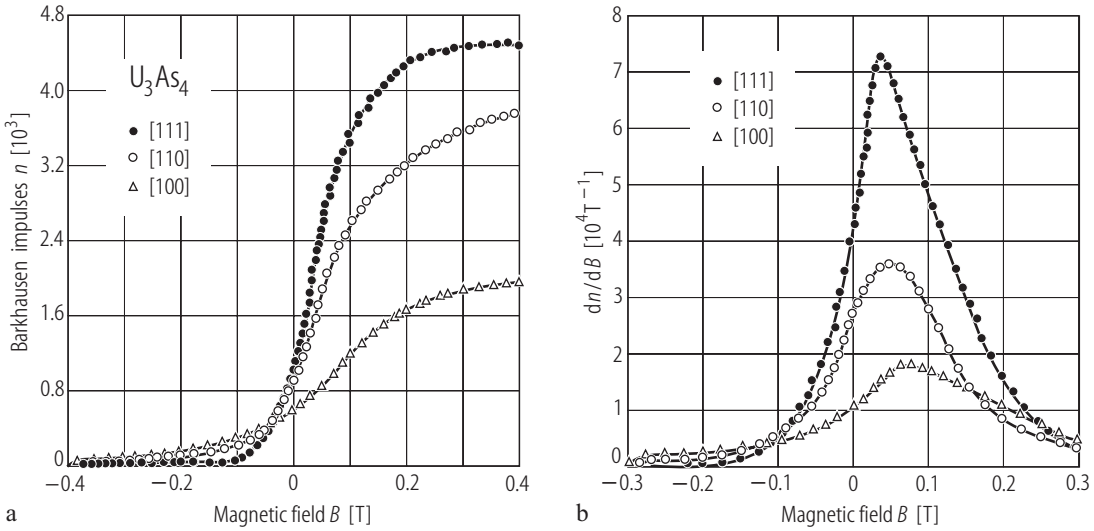

Fig. 146. U_3As_4, sc. Total number of Barkhausen impulses, n, vs. magnetic field, B, up to 0.4 T, taken at T = 77.4 K along the main crystallographic axes [77FMZ]. **(b)** Density of the occurrence of Barkhausen impulses, dn/dB, vs. magnetic field, B, measured as in panel **(a)** with two opposite field directions [77FMZ]. Note that the number n and therefore also the irreversible part of magnetization change increase more rapidly for B along easy direction.

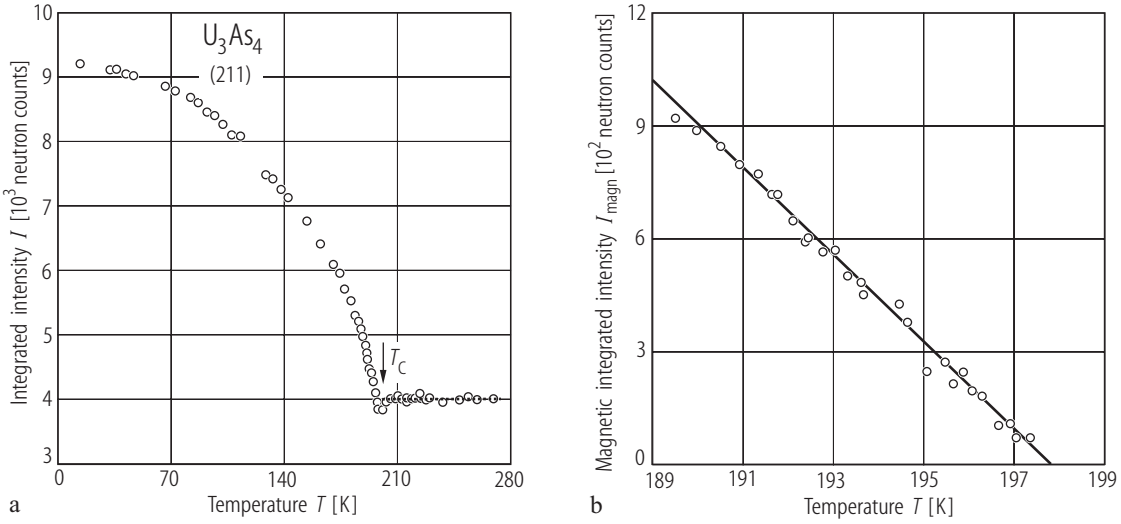

Fig. 147. U_3As_4, sc. **(a)** Total (211) nuclear and magnetic integrated neutron diffraction intensity, $I = I_N + I_{magn}$, vs. temperature, T [95SDTK]. The data were corrected for diffuse background scattering. Note a small minimum in the observed signal at the ferromagnetic phase transition at $T_C \approx$ 200 K. The dashed line marks the nuclear contribution, I_N, in the region 210 < T < 270 K. **(b)** Magnetic (211) integrated neutron diffraction intensity, I_{magn}, vs. T just below T_C as derived from $I(T)$ given in panel **(a)** by separating the nuclear scattering contribution I_N extrapolated down to 189 K. The solid line is a least squares fit of the data to the formula: $I_{magn} = At_-^{2\beta} + C_-t_-^{-\gamma} + C_+t_+^{-\gamma}$ which accounts for the spontaneous magnetization (first term) and critical scattering below and above the magnetic phase transition (second and third term, respectively) in terms of the reduced temperatures $t_- = (T - T_C)/T_C$ and $t_+ = (T_C - T)/T_C$. The best fit parameters: A = 21500±50, β = 0.49±0.02, T_C = 197.81±0.02 K, $C_- = C_+ = 0$. The obtained critical exponent β is close to the mean-field model value ($\beta = 0.5$).

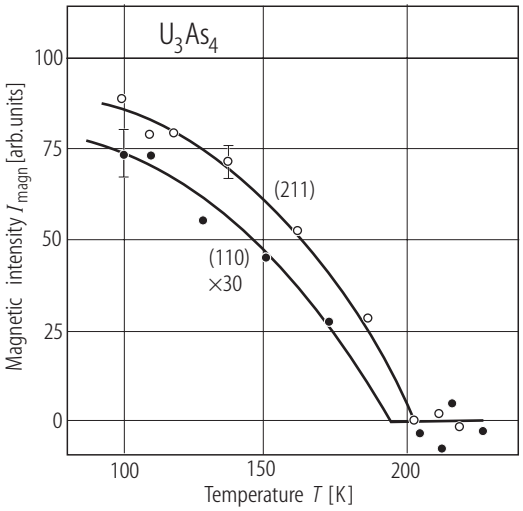

Fig. 148. U_3As_4, sc. Neutron diffraction intensity, I_{magn}, of a magnetic Bragg peak (211) and a superlattice peak (110) vs. temperature, T [81BRTH]. The (110) peak is not allowed by the space group $I\bar{4}3d$ and shows the same thermal variation as the magnetic peak (211) being thus purely magnetic in origin. Its presence unambiguously indicates a multiaxial magnetic structure. The ferromagnetic phase transition takes place at about 200 K into a noncollinear three-axial structure (see Fig. 188). At 4.2 K the uranium ordered moment amounts to 1.89(3) μ_B being in good agreement with the magnetization data (see Fig. 130).

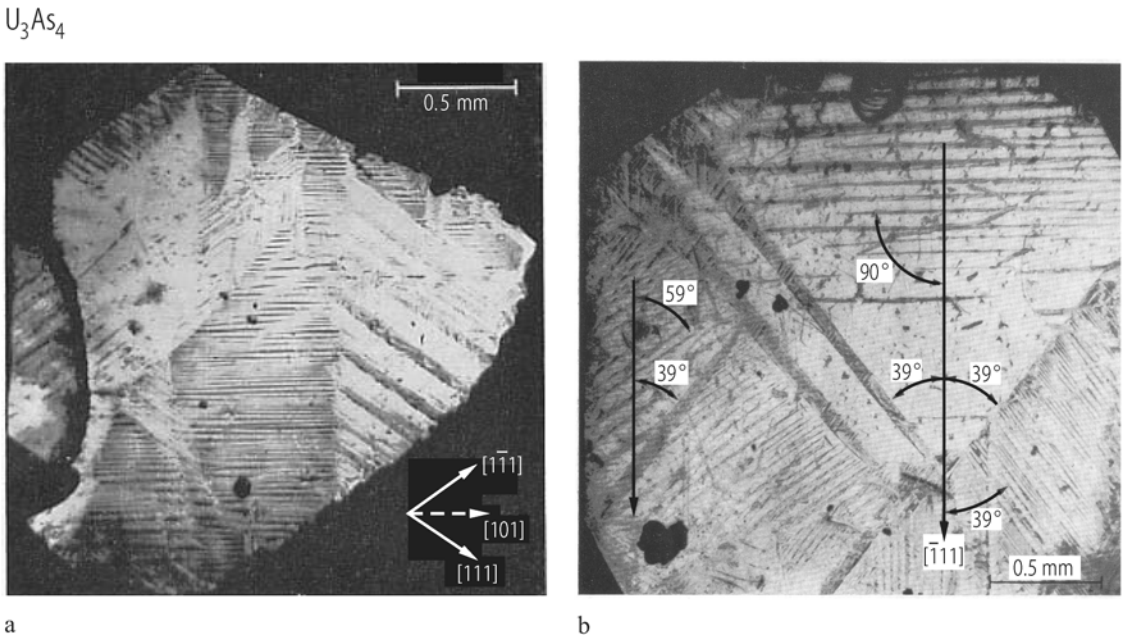

Fig. 149. U_3As_4, sc. Bitter patterns observed at 150 K by means of colloid technique on **(a)** (100) and **(b)** (211) natural surfaces [79GNM]. The pattern on (110) surfaces indicates the presence of parallel domains with 180° walls, which are interrupted by transverse "oblique" domains. The corresponding boundaries form 71° walls. The latter domains are often closed by a superficial strip structure lying along the [110] directions. On the (211) surface there are observed 180° Bloch walls lying along the only easy axis and a strip structure similar to that found on the (100) surface. Because of large anisotropy of the compound all the walls are very narrow.

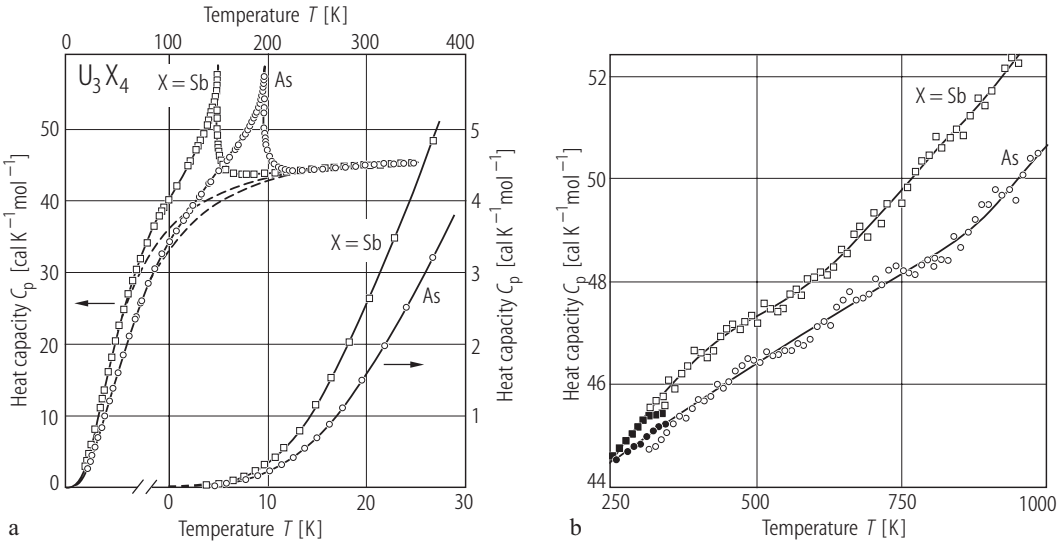

Fig. 150. U_3X_4, X = As, Sb. **(a)** Heat capacity, C_p, vs. temperature, T, in the range 5…350 K (left-hand side and top scales) and 5…30 K (right-hand side and bottom scales) [77AFWG]. Circles: U_3As_4; squares: U_3Sb_4. Sharp λ-shaped peaks manifest second-order ferromagnetic phase transitions at T_C = 196.1 and 147.5 K for the arsenide and antimonide, respectively. The solid lines are guides to the eye. The dashed lines represent the lattice contribution, C_L, calculated using a Debye function with the Debye temperature of 240 and 190 K for U_3As_4 and U_3Sb_4, respectively. The electronic specific heat coefficient $\gamma(0)$ was estimated to be 3.77 and 1.67 mJ/(K^2 mol U) for U_3As_4 and U_3Sb_4, respectively. These values are certainly too small if one compares them with those of U_3P_4 and U_3As_4 given in Fig. 41. **(b)** Heat capacity, C_p, vs. temperature, T, in the range 250…950 K [77AFWG]. Circles: U_3As_4; squares: U_3Sb_4. Full symbols are used to mark the data, which overlap with those from panel **(a)**.

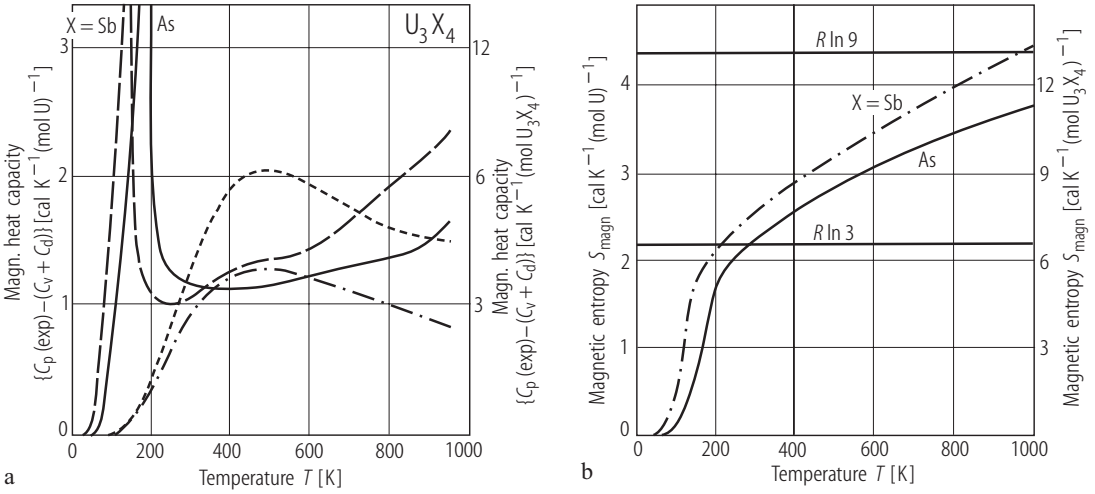

Fig. 151. U_3X_4, X = As, Sb. **(a)** Magnetic contribution to the heat capacity, C_{magn}, vs. temperature, T, calculated by subtracting from the $C_p(T)$ data, given in Fig. 150, the lattice contribution, C_L, (see Fig. 150) and the dilatational term, $C_d = C_p - C_v$, estimated from the Nernst-Lindemann expression with the melting temperature T_m = 1700 K [77AFWG]. Solid line: U_3As_4; long-dashed line: U_3Sb_4. The short-dashed line represents a Schottky contribution in a crystal field model proposed by [71TMS] for D_{2d} symmetry. The dashed-dotted line is a fit with the triplet ground state. Note however that such a ground state is unlikely for the S_4 point symmetry of uranium atoms (see Fig. 35) but it could be consistent with the three close lying singlets as shown in Fig. 71a in the case of U_3P_4. **(b)** Magnetic entropy, S_{magn}, vs. temperature, T, derived from the results presented in panel **(a)** [77AFWG]. Solid line: U_3As_4; dashed line: U_3Sb_4. At high temperatures $S_{magn}(T)$ approaches the limiting value of $R\ln 9$ for the $^3H_4$ ground term of U^{4+} ion. The excess entropy associated with ferromagnetic ordering amounts to about 9.3 and 9.45 J/(K mol U) for U_3As_4 and U_3Sb_4, respectively. See also [77WG].

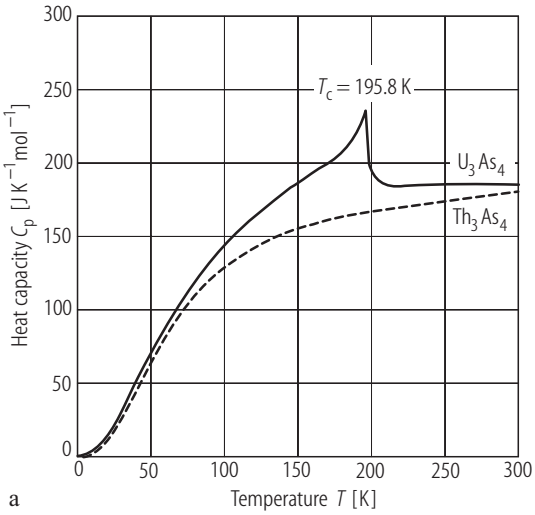

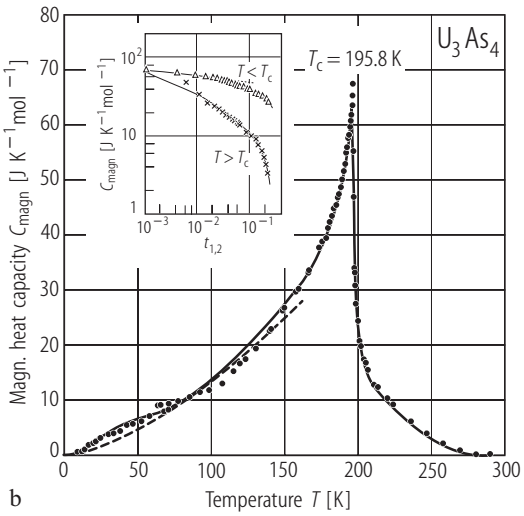

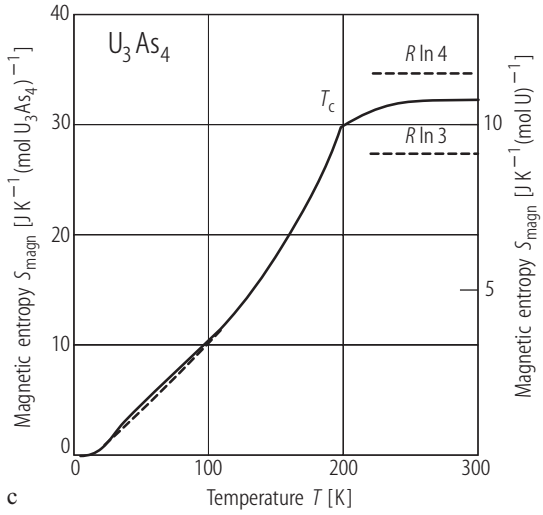

Fig. 152. U_3As_4, Th_3As_4. **(a)** Heat capacity, C_p, vs. temperature, T [80BLTH]. A pronounced λ-shaped anomaly at T_C = 195.8 K manifests the onset of ferromagnetism in U_3As_4. The nonmagnetic Th_3As_4 exhibits a usual sigmoidal shape of $C_p(T)$ without any anomaly yielding the electronic specific heat coefficient $\gamma \approx 0$ and the Debye temperature Θ_D = 262 K. **(b)** Magnetic contribution to the heat capacity, C_{magn}, vs. temperature, T, (solid line) calculated by subtracting from the $C_p(T)$ data, given in panel **(a)**, the lattice term, C_L,and the dilational term, $C_p - C_v$, both equal to those found for Th_3As_4 (see Fig. 152a, and the electronic term, $C_e = <\gamma>T$, with $<\gamma>_{RT}$ = 14 mJ/(mol K^2), derived from the difference in the heat capacity of U_3As_4 and Th_3As_4 at room temperature [80BLTH]. The full circles are the experimental data taken from [77AFWG]. Note an unusual behaviour of $C_{magn}(T)$ in the range 10…70 K, attributed to a complex low-temperature spin wave spectrum in the compound with multiaxial magnetic structure. The dashed line represents a spin-wave dependence $aT^{3/2}$. Inset: C_{magn}, vs. reduced temperature, t, (in double-logarithmic scale), defined as $t_1 = 1 - T/T_C$ for $T < T_C$ and $t_2 = 1 - T_C/T$ for $T > T_C$ where T_C = 195.8 K. Triangles and crosses are the experimental data for $T < T_C$ and $T > T_C$, respectively. The dotted line is a linear asymptote $C_{magn} = A't^{-\alpha'}$ of the $T < T_C$ data in the range $10^{-3} < t_1 < 2 \cdot 10^{-2}$ with the exponent α' = 0.08. For $T > T_C$ the data in the range $10^{-3} < t_2 < 2 \cdot 10^{-1}$ follow the dependence $C_{magn} = At^{-\alpha} + B$ with the critical coefficient α = 0.125. For the values of A', A and B and comparison with theoretical predictions for S = ½ Ising models see Table I. **(c)** Magnetic entropy, S_{magn}, vs. temperature, T, derived from the results presented in panel **(b)** [80BLTH]. The total magnetic entropy at 300 K is 11.0 J/(K mol U), i.e. larger than Rln3 but smaller than Rln4 (see the dashed lines). The rather high value of S_{magn} suggests that a pseudodoublet is the CF ground state and a pseudodoublet is the first excited state separated by an energy lower than k_BT_C (compare Fig. 151b).

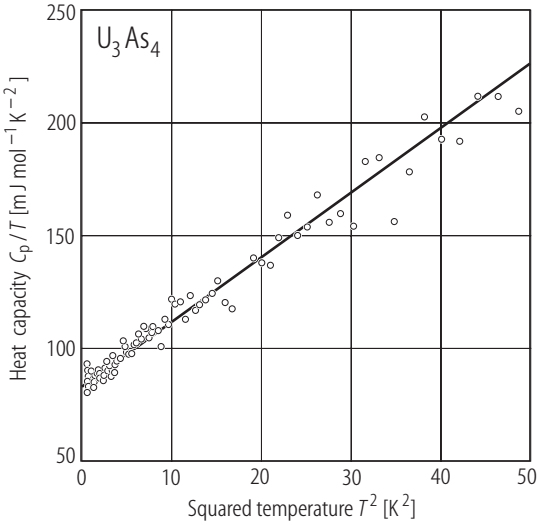

Fig. 153. U_3As_4. Heat capacity over temperature, C_p/T, vs. squared temperature, T^2, in the range T = 0.6…7 K [01IWMA]. The solid line is a fit to the expression $C/T = \gamma(0) + \beta T^2$ yielding $\gamma(0)$ = 83 mJ/mol K^2. This value is considerably larger than $\gamma(0)$ = 3.77 mJ/mol K^2, obtained in [77AFWG] (see Fig. 150), and three times larger than the theoretical value of 28 mJ/mol K^2, derived in [99AHYP] (see Fig. 27).

For Fig. 155 see next page

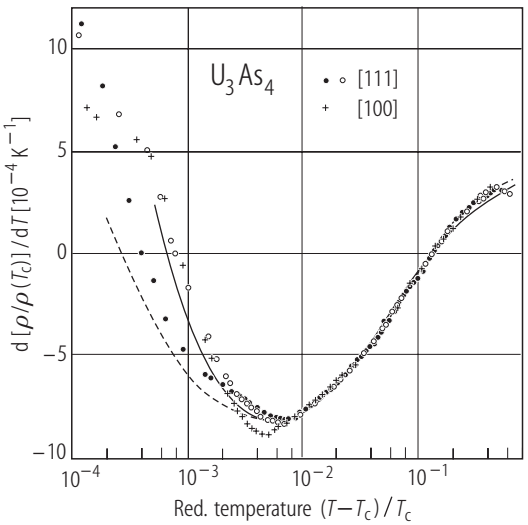

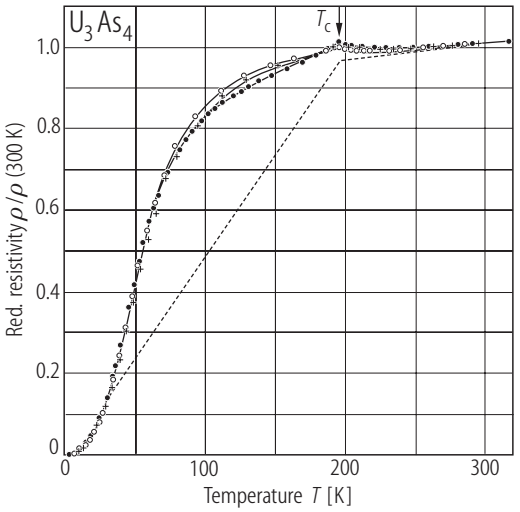

Fig. 154. U_3As_4, sc. Normalized electrical resistivity, ρ/ρ(300K), vs. temperature, T, measured along the [100] (open circles), [110] (full circles) and [111] (crosses) directions [71HB]. At 300 K the resistivity was equal to 499, 491 and 499 μΩcm, for the [100], [110] and [111] directions, respectively. Note a slightly anisotropic behaviour of $\rho(T)$, solely at higher temperatures in the ordered state, which is considerably smaller than that observed for U_3P_4 (compare Fig. 98). The resistivity measured along the [110] and [111] directions shows in the ferromagnetic region a large dependence on magnetic and thermal history of the sample (not shown). This becomes different for various samples because of magnetic domain effect. The strongly convex shape of $\rho(T)$ below T_C points to the presence of additional boundaries in the Brilloiun zone, related to the polyaxial magnetic structure. The dashed line approximates the relation $\rho(T) = \rho_0^{\infty} \frac{T}{T_C} + BT$ for $T < T_C$ and $\rho(T) = \rho_0^{\infty} + BT$ for $T > T_C$, where ρ_0^{∞} is the spin disorder resistivity and the term BT describes the phonon contribution to the total resistivity.

←

Fig. 156. U_3As_4, sc. Temperature derivative of the normalized electrical resistivity, d[$\rho/\rho(T_C)$]/dT, vs. normalized temperature, $(T–T_C)/T_C$ (note a logarithmic scale), in the paramagnetic region [80H3]. Crosses: $i \parallel$ [100]; open and full circles: $i \parallel$ [111]. The dashed and solid lines are the least-squares fits to the formula comprising the residual, phonon and magnetic contributions to the resistivity, calculated using different values of the critical exponent υ = 0.55 and 0.6 (for details see the original paper). The universal behaviour is well seen for temperatures about 2 K higher than T_C.

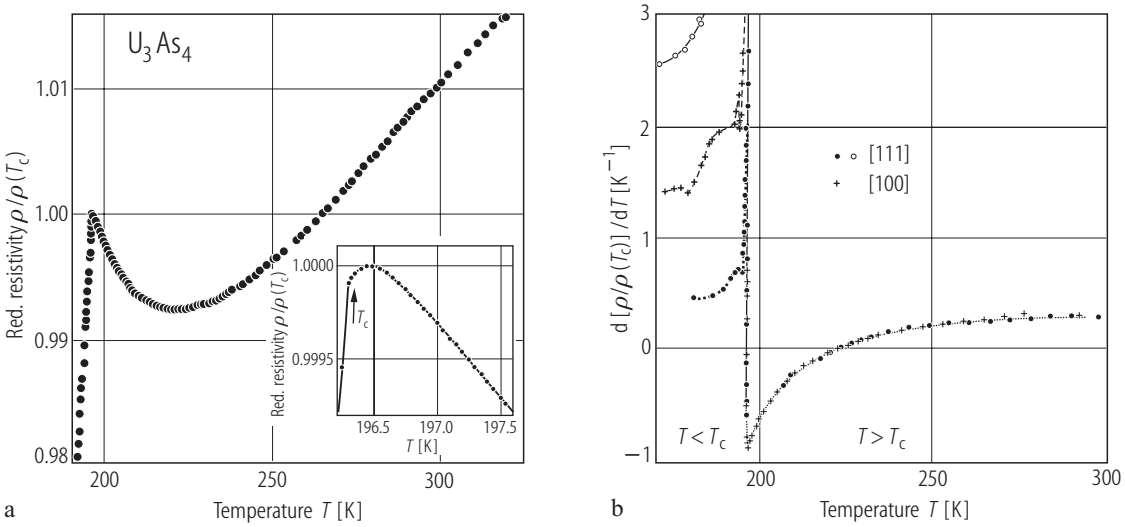

Fig. 155. U_3As_4, sc. **(a)** Normalized electrical resistivity, $\rho/\rho(T_C)$, measured along the [111] direction vs. temperature, T, in the range 190…320 K [80H3]. T_C = 196.3(3) K. Inset: $\rho/\rho(T_C)$ in the very vicinity of T_C. **(b)** Temperature derivative of the normalized electrical resistivity, $d[\rho/\rho(T_C)]/dT$, vs. temperature, T, in the range 170…300 K measured for three different samples [80H3]. Full circles and dots: two samples along the [111] axis; crosses: one sample along the [100] axis. Note a universal behaviour in the paramagnetic region (see also Fig. 156) and pronounced differences in the ordered region caused by domain effects.

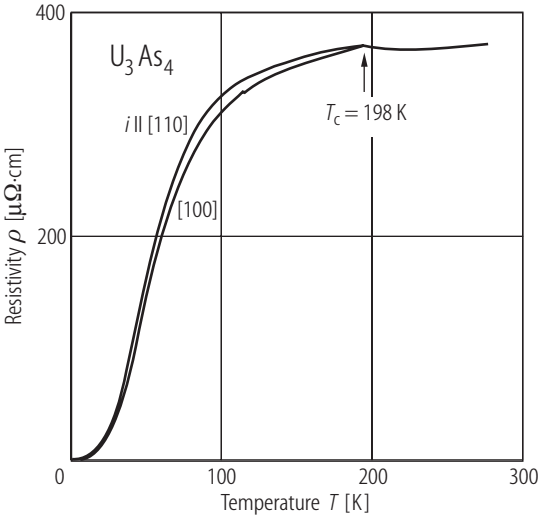

Fig. 157. U_3As_4, sc. Electrical resistivity, ρ, vs. temperature, T, down to 0.4 K measured with the current flowing along the [100] (lower curve) and [110] (upper curve) directions [01IWMA]. RRR is 730 and the residual resistivity ρ_0 is 0.5 μΩcm along [100] and 540 and 0.7 μΩcm, respectively, along [110]. These values indicate a superior quality of the samples measured. In the paramagnetic region the resistivity is isotropic, as expected for a cubic crystal structure. The arrow marks the ferromagnetic phase transition at T_C = 198 K. Below 4 K the resistivity follows an AT^2-dependence with A = 0.028 and 0.025 μΩcm/K^2 along [100] and [110], respectively.

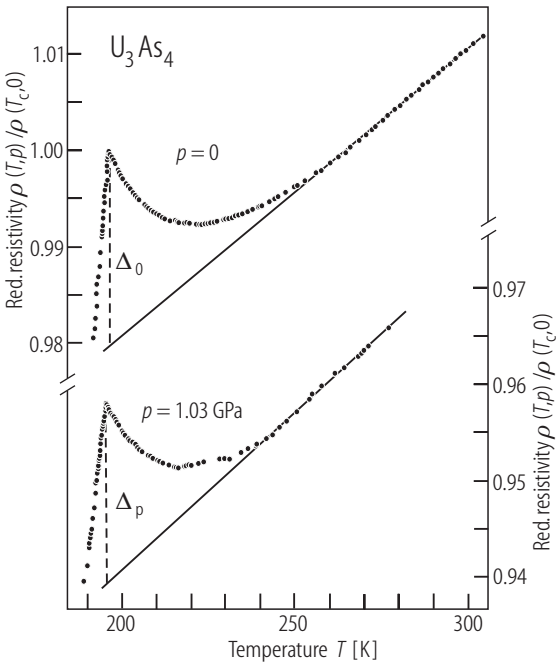

Fig. 158. U_3As_4, sc. Normalized electrical resistivity, $\rho(T,p)/\rho(T_C,0)$, vs. temperature, T, measured along the [100] axis in the vicinity of T_C and in the paramagnetic range at ambient pressure (upper curve) and at hydrostatic pressure p of 1.03 GPa (lower curve) [86HMD]. The solid lines mark a straight-line behavior of the resistivity at high temperatures and define the value of Δ_i (i = 0, p; dashed bars), which is a measure of the Fermi wave vector in ferromagnetic semimetals (see Fig. 46). The absolute value of the resistivity decreases with increasing pressure. At 300 K, $1/\rho(d\rho/dp)$ is –0.37 GPa^{-1}. The Curie temperature decreases under pressure with the rate of –1.5 K/GPa. From the change of Δ_i under pressure the mutual shift of the conduction and valence bands was estimated to be of about 2.6 meV/GPa.

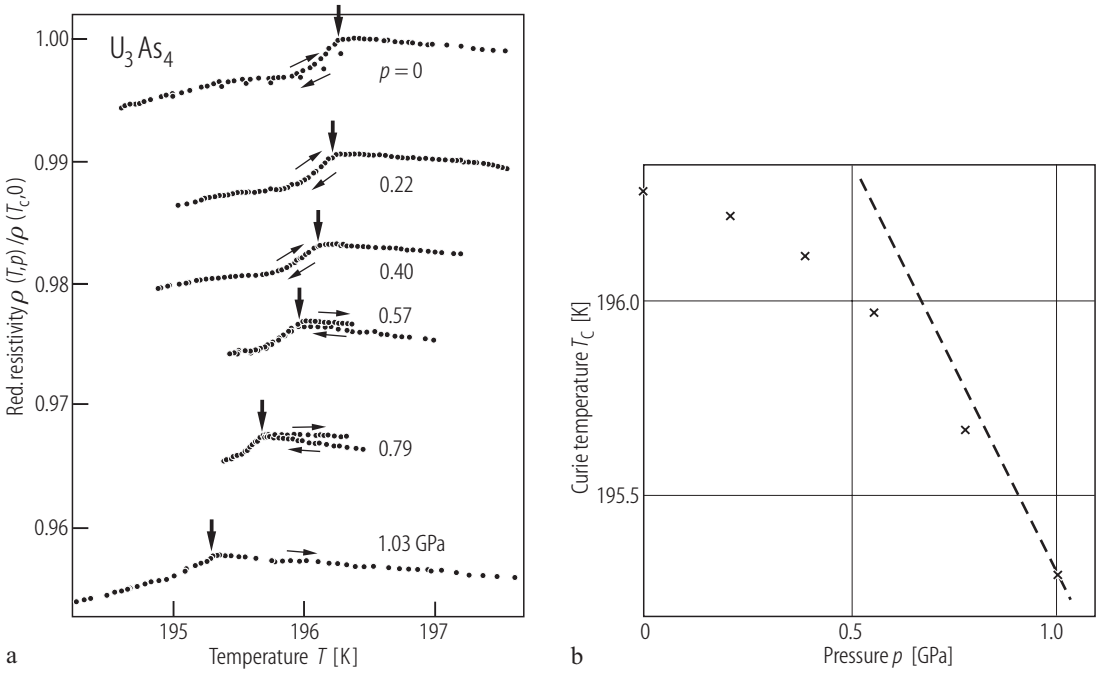

Fig. 159. U_3As_4, sc. **(a)** Normalized electrical resistivity, $\rho(T,p)/\rho(T_C,0)$, vs. temperature, T, in the vicinity of T_C, measured along the [100] axis under various hydrostatic pressures, p, up to 1.03 GPa [86HMD]. The vertical bold arrows mark T_C. Some irreversibility in the resistivity taken on cooling and heating (as indicated by the thin arrows) was caused by instabilities of the electrical contacts. **(b)** Curie temperature, T_C, vs. hydrostatic pressure, p, determined from the electrical resistivity measurements [86HMD]. The dashed line marks the behavior derived from the T_C vs. U-U distance dependence found for the U_3As_4-reach solid solutions with U_3P_4 (see Fig. 42), where the compressibility $dD_{UU}/dp = 5.1 \cdot 10^{-3}$ GPa^{-1} was assumed as in the case of U_3P_4. The slope of this line is –1.5 K/GPa.

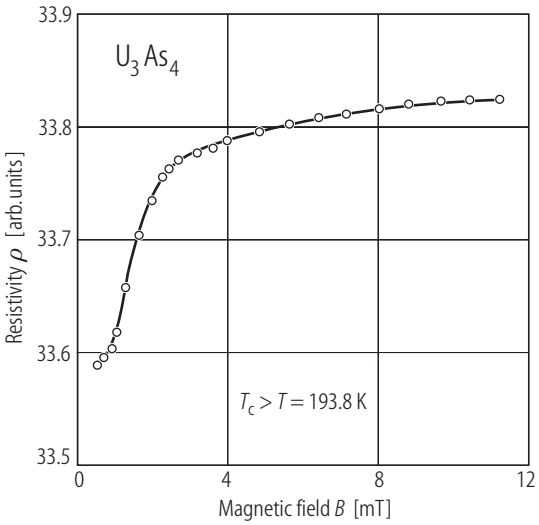

Fig. 160. U_3As_4, sc. Electrical resistivity, ρ (arb. units), vs. magnetic field, B, up to 0.012 T, measured at T = 193.8 K (below T_C) with $i \parallel [111]$ and $B \parallel [111]$ [77HK]. The resistivity increases with increasing B and tends to saturation in higher fields, probably due to magnetic domain processes.

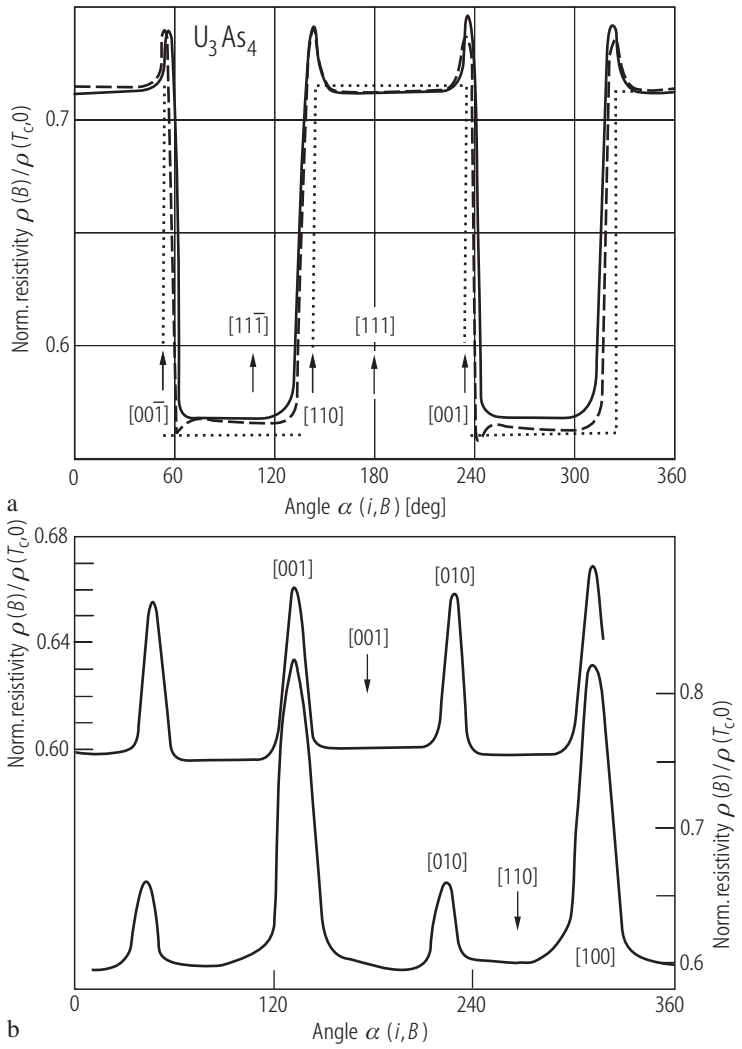

Fig. 161. U_3As_4, sc. **(a)** Normalized electrical resistivity, $\rho(B)/\rho(T_C,0)$, vs. angle $\alpha(i,B)$ between the current, i, and the magnetic field, B, measured at T = 78 K in a constant magnetic field B = 0.69 T, with $i \parallel [111]$ and B rotating in the plane $(\bar{1}\,10)$ [80H1]. $\rho(T_C,0)$ is the zero field resistivity at the Curie temperature.The solid and dashed curves are the experimental data for two different single crystals. The dotted line is the calculated variation obtained assuming strong domain anisotropy (for the details see the original paper). Differences between the experimental and calculated results, observed near main crystallographic directions [001], [110] or $[00\,\bar{1}]$ are attributed to polydomain structure forming in some ranges of $\alpha(i,B)$. **(b)** $\rho(B)/\rho(T_C,0)$ vs. $\alpha(i,B)$ taken as in panel **(a)** but with $i \parallel [100]$ and B rotating either in the (100) plane (upper curve) or in the (001) plane (lower curve) [80H]. The resistivity maxima near [100]-type axes are due to the presence of domain walls in a polydomain crystal.

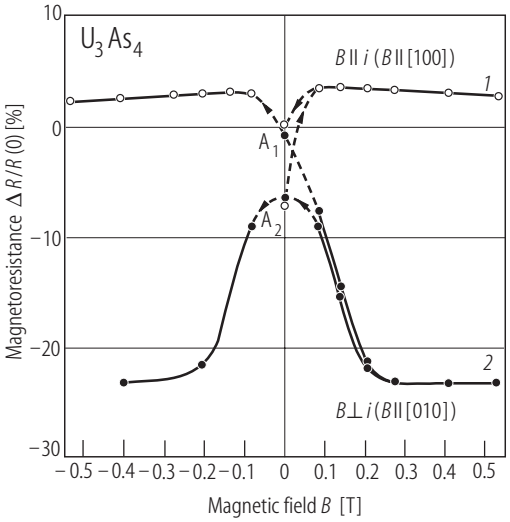

Fig. 162. U_3As_4, sc. Transverse and longitudinal magnetoresistance, $\Delta R/R(0)$, vs. magnetic field, B, up to 0.53 T, measured at $T = 77$ K with the current flowing along the [100] direction and B applied along the [100] axis (open circles) and along the [010] axis (full circles) [71HB]. Upon initial cooling in zero field $\Delta R/R(0)$ has a value denoted as A_2 but it changes to A_1 when the field $B \parallel i$ is increased to 0.5 T and then is switched off. Upon the field rise up to 0.53 T and then decrease back to zero for $B \perp i$ the value of $\Delta R/R(0)$ at $B = 0$ is again equal to A_2. The change in the sign of the field yields symmetrical curves for both crystallographic directions.

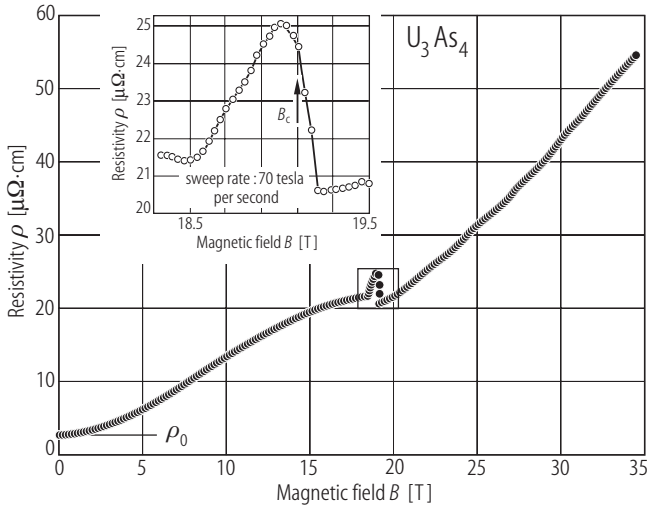

Fig. 163. U_3As_4, sc. Electrical resistivity, ρ, vs. magnetic field, B, up to 35 T, measured at $T = 4.2$ K with $i \parallel [110]$ and $B \parallel [001]$ [94BWHF]. Note a peak in the resistivity at $B_c = 19.1$ T, which corresponds to the jump in the magnetization (see Fig. 140) and is caused by a spin reorientation from noncollinear ferromagnetic structure with the [111] easy axis to a high-field phase, which is considered to be collinear ferromagnetic with the moments aligned along the [100] axis. An apparent asymmetry in the peak (see the inset) probably results from some magnetic disorder at the phase transition. However, in view of a detailed symmetry analysis made by [00KSK] this phase cannot be collinear but rather should be as that presented in Fig. 36b.

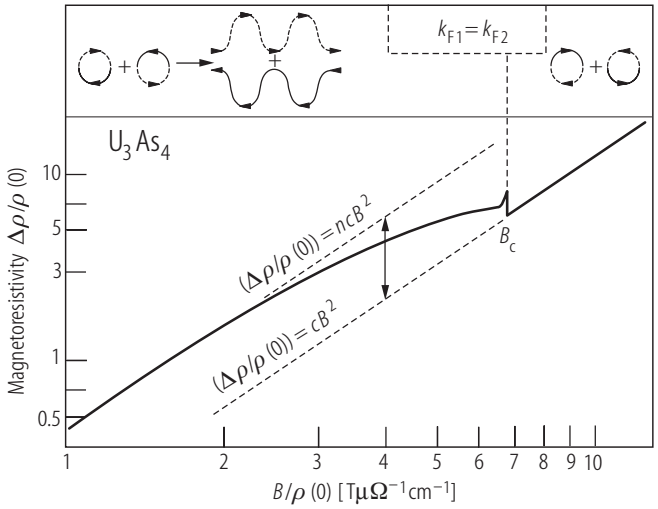

Fig. 164. U_3As_4, sc. Transverse magnetoresistivity, $\Delta\rho/\rho(0)$, vs. magnetic field over zero-field resistivity, $B/\rho(B{=}0)$, measured at $T = 4.2$ K with $i \parallel [110]$ and $B \parallel [001]$ (Kohler's plot) [94BWHF]. The dashed lines mark a B^2 dependence of $\Delta\rho/\rho(0)$, both above and much below the spin reorientation transition at $B_c = 19.1$ T (see Fig. 163). On approaching B_c from low fields the magnetoresistivity saturates. The observed behaviour is interpreted in terms of a compensated character of the band structure and its fractional polarization (see the original paper). The upper panel presents schematically the prediction of Cabrera and Falicov theory: in the compensated case there are one-electron (solid line) and one-hole (dotted line) orbits, denoted by vectors k_{F1} and k_{F2}, respectively, which transform at high magnetic fields first into open orbits and then back to closed orbits above B_c.

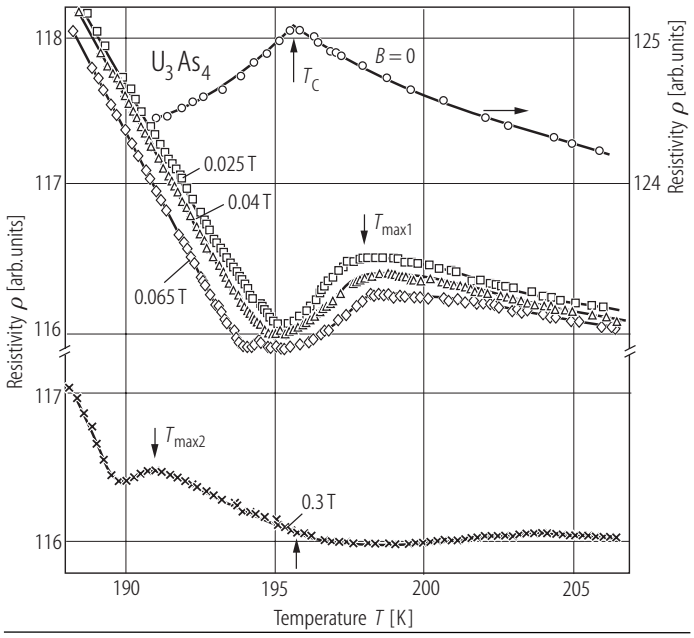

Fig. 165. U_3As_4, sc. Electrical resistivity, ρ (arb. units), vs. temperature, T, measured in the vicinity of the Curie point with $i \parallel$ [100] and in an applied magnetic field $B \parallel$ [100] [73HK2]. Circles: B = 0; squares: 0.025 T; triangles: 0.04 T; diamonds: 0.065 T; crosses: 0.3 T. Note different vertical scales. In external field at the temperature T_{max1} above T_C = 196 K there occurs a maximum in $\rho(T)$, which shifts, broadens and finally vanishes with increasing B. This behaviour is interpreted in terms of scattering of conduction electrons on spatial magnetization fluctuations. Note in the lower panel that there also appears in $\rho(T)$ another maximum at the temperature T_{max2} below T_C, which increases and shifts to lower temperatures when the magnetic field strength rises (not shown). The origin of this feature is unknown.

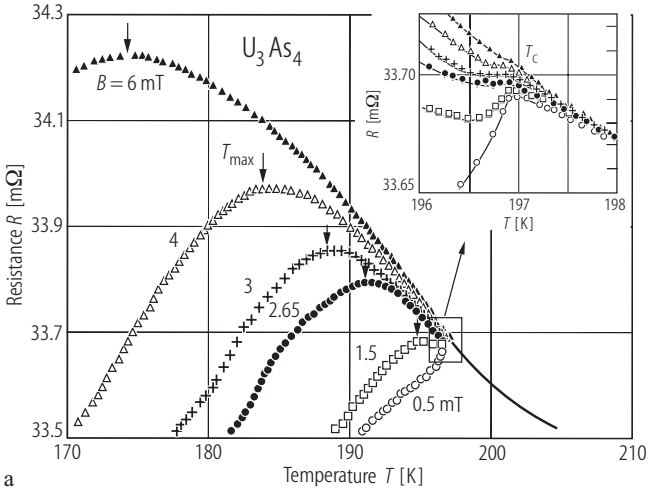

a

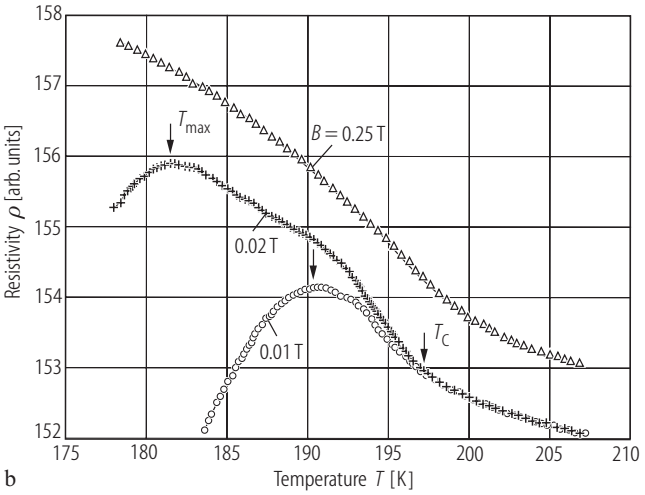

b

Fig. 166. U_3As_4, sc. **(a)** Electrical resistance, R, vs. temperature, T, near the Curie point, measured with $i \parallel$ [111] in very weak magnetic fields $B \parallel$ [111] [77HK]. Open circles: B = 0.5 mT; squares: 1.5 mT; full circles: 2.65 mT; crosses: 3 mT; open triangles: 4 mT; full triangles: 6 mT. Inset: $\rho(T)$ in the very vicinity of T_C. **(b)** ρ vs. T measured as the data from panel **(a)** but in stronger magnetic fields [73HK2]. Circles: 0.01 T; crosses: 0.02 T; triangles: 0.25 T. Note a maximum in $\rho(T)$ at T_{max} below T_C that shifts to lower temperatures with increasing magnetic field strength. Its appearance is attributed to scattering of free carries by critical magnetic fluctuations (compare Fig. 165).

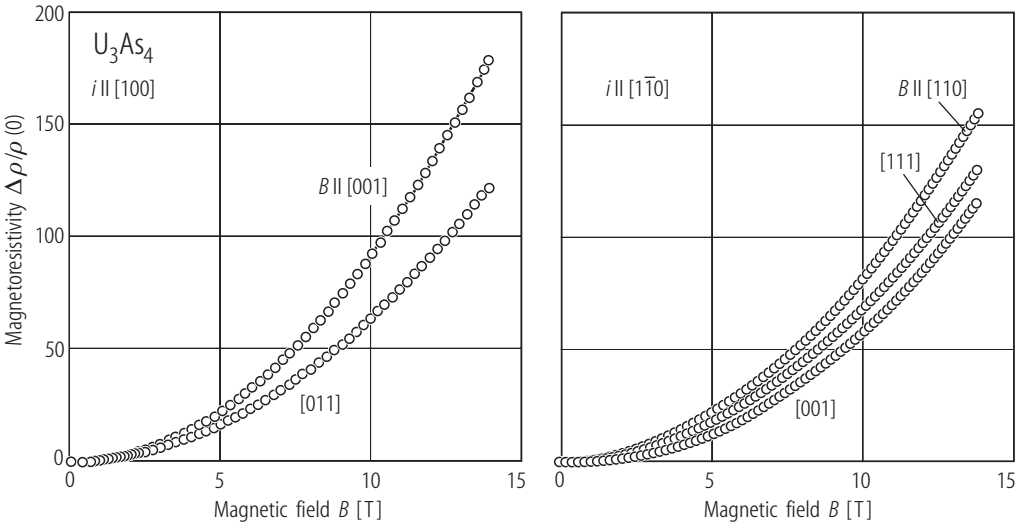

Fig. 167. U_3As_4, sc. Magnetoresistivity, $\Delta\rho/\rho(0)$, vs. magnetic field, B, measured at $T = 0.45$ K with the electrical current flowing along the [100] (left-hand side panel) and [1 $\bar{1}$ 0] (right-hand side panel) directions and magnetic fields applied along the principal crystallographic axes [01IWMA]. For any field direction $\Delta\rho/\rho(0)$ increases with increasing field, approximately as B^2. This behaviour strongly indicates that the compound is a compensated metal with all cyclotron orbits closed, which is in line with the presence of four molecules in the unit cell and thus the even number of valence electrons.

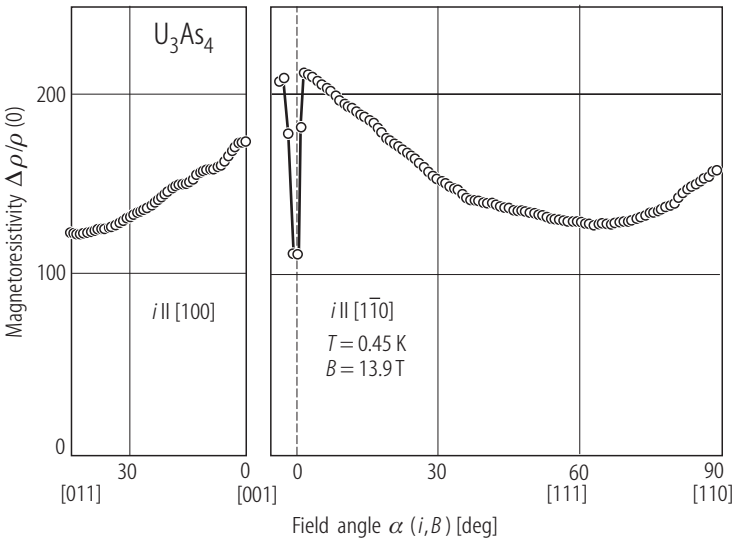

Fig. 168. U_3As_4, sc. Magnetoresistivity, $\Delta\rho/\rho(0)$, vs. angle $\alpha(\boldsymbol{B},\boldsymbol{i})$ between magnetic field and electrical current, measured at $T = 0.45$ K in the magnetic field of 13.9 T with the current flowing along the [100] axis (left-hand side panel) and the [1 $\bar{1}$ 0] axis (right-hand side panel) [01IWMA]. A sharp dip at $B \parallel [001]$, found for $i \parallel [1\,\bar{1}\,0]$, may suggest the existence of open orbits. However, in such a case a saturation tendency in the $\Delta\rho/\rho(0)$ vs. B variation should occur, which is not observed experimentally (see Fig. 167).

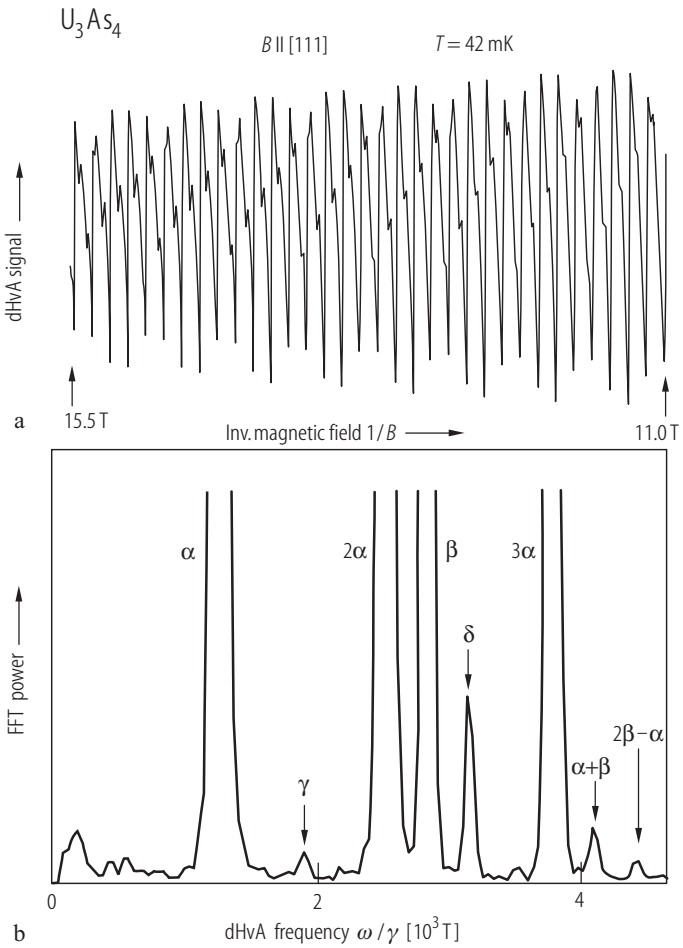

Fig. 169. U_3As_4, sc. **(a)** dHvA oscillations measured at $T = 42$ mK in magnetic fields ranging from 11 to 15.5 T applied along the [111] axis [01IWMA]. **(b)** Fast Fourier transform spectrum corresponding to the data from panel **(a)** [01IWMA]. Note the presence of four fundamental branches labeled α, β, γ and δ in the frequency range from $1.3 \cdot 10^3$ to $3.2 \cdot 10^3$ T. The other features are higher harmonics, sum and difference components of the fundamental branches. For the angular dependence of the dHvA frequencies see Fig. 170.

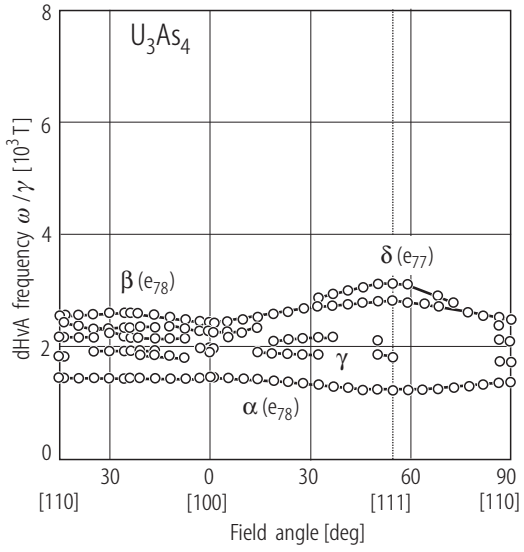

Fig. 170. U_3As_4, sc. Angular dependence of the dHvA frequencies measured as in Fig. 169 [01IWMA]. The branches α and β, observed in the whole angular region, imply closed Fermi surfaces. These two branches were detected also in earlier dHvA studies [94IAKI]. The branch δ was not observed in the whole angular range, probably because of the curvature factor of the Fermi surface or very large cyclotron mass. The effective cyclotron mass is 5.1 m_0, 15 m_0 and 70 m_0 for the branch α, β and δ, respectively. The mean free path for these branches is as large as 290, 370 and 210 nm, respectively, indicating high quality of the single crystal studied (see also Fig. 157). The Dingle temperatures are small (0.03…0.23 K). For Brillouin zone and cross sections of the theoretical Fermi surfaces calculated by [99AHYP] see Fig. 29. The origin of each dHvA branch is as follows: branch α – e_{78} (an inner orbit of the band 78-electron surface centered at Γ); branch β – e_{78} (an outer orbit of the band 78-electron surface centered at Γ); branch δ – e_{77} (a band 77-electron surface centered at Γ). Some other branches may originate from a complicated band 76-hole Fermi surface, named h_{76}.

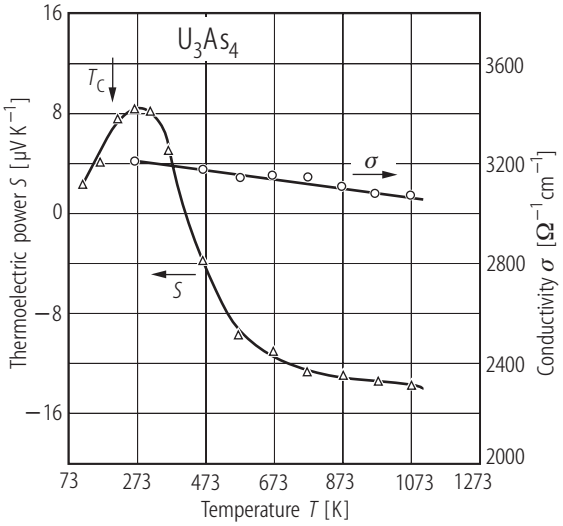

Fig. 171. U_3As_4. Electrical conductivity, σ, (circles; right-hand scale) and thermoelectric power, S, (triangles; left-hand scale) vs. temperature, T, in the range 120…1070 K [64WP2]. Around T = 273 K $S(T)$ goes through a positive maximum, and above 420 K it becomes negative. This characteristic temperatures are lower by 40 K from those presented in Fig. 112.

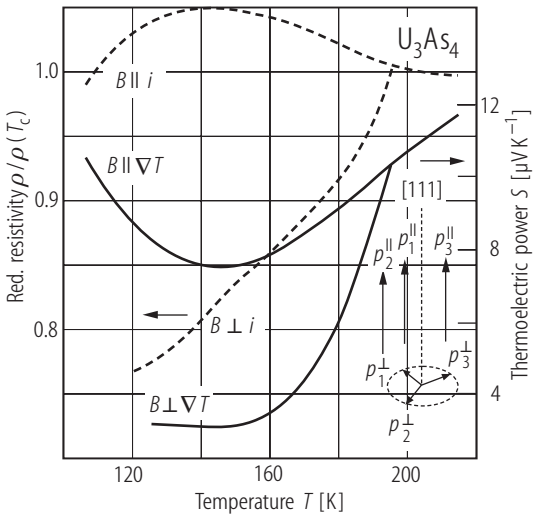

Fig. 172. U_3As_4. Normalized electrical resistivity, $\rho/\rho(T_C)$ (dashed lines, left-hand side scale), and thermoelectric power, S (solid lines, right-hand side scale), vs. temperature, T, measured in a magnetic field of 0.85 T applied parallel and perpendicular to the direction of the current, i, or the gradient of temperature, ∇T [97WH]. Inset: schematic representation of the magnetic structure projected onto the [111] axis and on the (111) plane (for detailed description of the magnetic structure see Fig. 36). In the paramagnetic state the resistivity and the thermopower are isotropic. In the ordered region the resistivity shows an anisotropic behaviour. The ratio $\rho(B \parallel i)/\rho(B \perp i)$ reaches its maximum value of 1.32 at 124 K. The observed anisotropy is likely due to the spin polarization of the conduction bands. The thermoelectric power is positive and the ratio $S(B \parallel i)/S(B \perp i)$ monotonically increases with decreasing temperature.

For Fig. 173 see next page

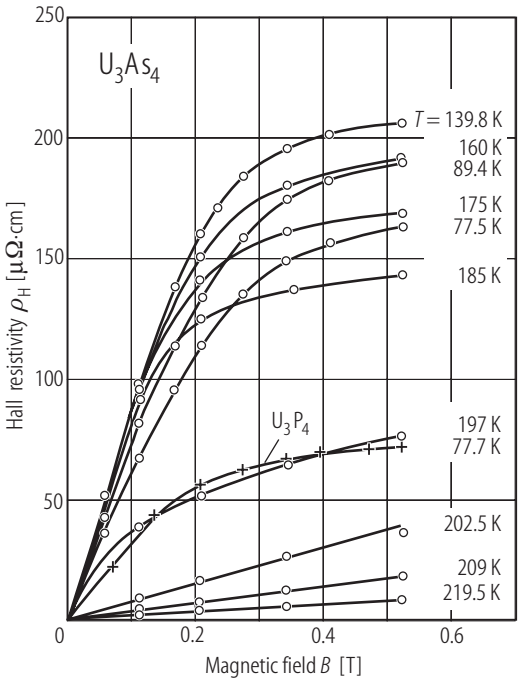

Fig. 174. U_3As_4. Hall resistivity, ρ_H, vs. magnetic field, B, at various temperatures in the range 77…220 K [72H]. For comparison there is shown $\rho_H(B)$ for U_3P_4 measured at T = 77.7 K. Circles: U_3As_4; crosses: U_3P_4.

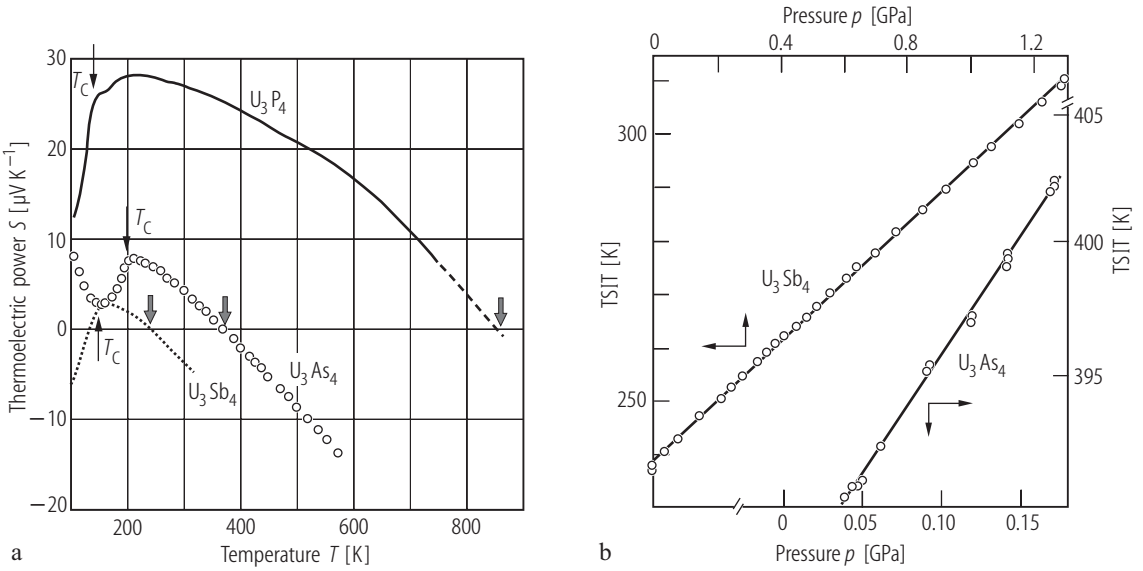

Fig. 173. U_3X_4, X = As, Sb, sc. **(a)** Thermoelectric power, S, vs. temperature, T, in the range 100…580 K for U_3As_4 (open circles) and 100…320 K for U_3Sb_4 (dots) [86HMD]. For comparison $S(T)$ for U_3P_4 in the range 100…750 K is also shown (solid line). The thin arrows mark T_C. The bold arrows mark the temperature TSIT of the inversion of the sign of TEP (in the case of U_3P_4 TSIT was estimated by extrapolation of $S(T)$ to higher temperatures). TSIT = 870, 389 and 237 K for U_3P_4, U_3As_4 and U_3Sb_4, respectively. **(b)** TSIT vs. hydrostatic pressure, p, up to 0.16 GPa for U_3As_4 and 1.3 GPa for U_3Sb_4 [86HMD]. Note different scales for the two compounds. The solid lines serve as a guide to the eye. The value of TSIT depends essentially on the electron concentration but also on the relative strength of magnetic and phonon scattering as well as on the effective masses of electrons and holes.

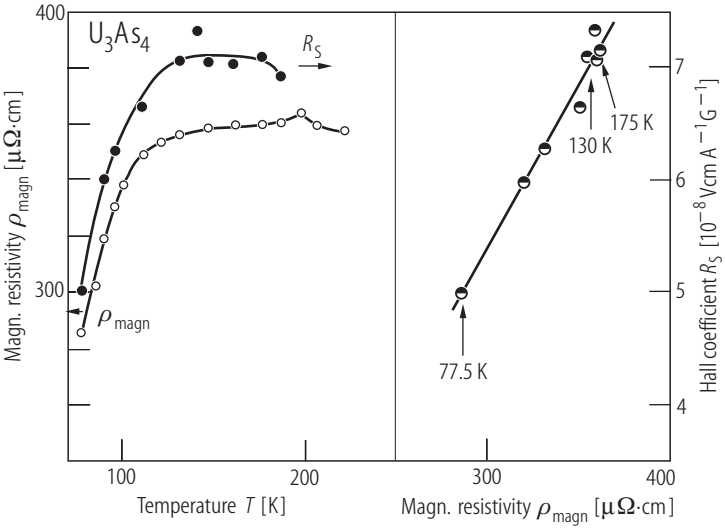

Fig. 175. U_3As_4. Anomalous Hall coefficient, R_s, vs. temperature, T, in the range 80…180 K (right-hand side scale) [72H]. For comparison the magnetic part of the resistivity, $\rho_{magn}(T)$, is also shown (left-hand side scale). Note that R_s is proportional to ρ_{magn} in the range 77…175 K, as emphasized in right-hand side panel.

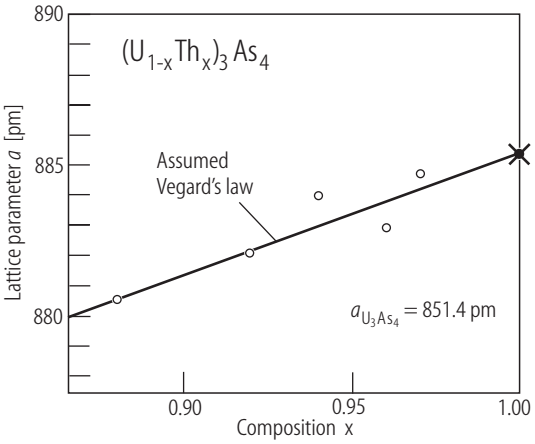

Fig. 176. $(U_{1-x}Th_x)_3As_4$. Cubic lattice parameter, a, vs. Th content, x [77MBH]. The solid line marks Vegard's law.

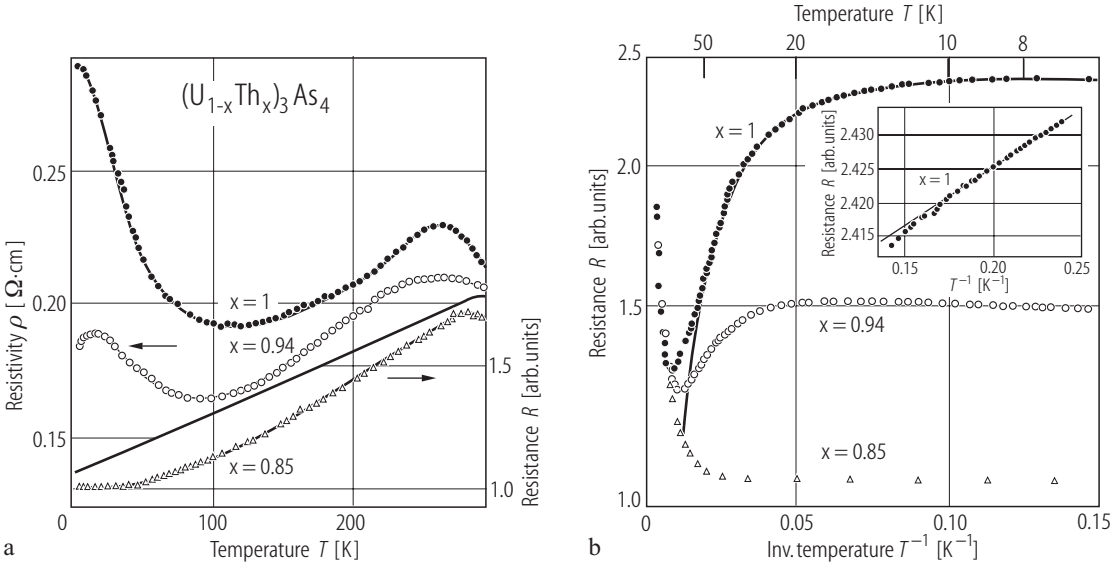

Fig. 177. $(U_{1-x}Th_x)_3As_4$. **(a)** Electrical resistivity, ρ, vs. temperature, T, for x = 1 (full circles), 0.94 (open circles) and 0.85 (triangles) [79MHW2]. Note that the right-hand scale for the x = 0.85 solid solution is the resistance, R (arb. units). For all three samples the temperature coefficient of the resistivity changes its sign from positive to negative near room temperature in a manner characteristic of heavily doped semiconductors (broad maxima). **(b)** Resistance, R (arb. units), vs. inverse temperature, $1/T$, in the range 4.2…100 K for the samples from panel **(a)** [79MHW2]. Note a logarithmic vertical scale. The solid line is a fit of the experimental $R(T)$ for nominally pure Th_3As_4 sample (x = 1) to the Mott's expression $1/R = A_1\exp(-\varepsilon_1/kT) + A_2\exp(-\varepsilon_2/kT) + A_3\exp(-\varepsilon_3/kT)$ with the parameters: ε_1 =11 meV, ε_2 = 3.8 meV and ε_3 = 0.0062 meV, denoting respectively: the activation energy of an electron from impurity band or level to the conduction band, the activation energy of an electron from the localized impurity states to the extended states near the Fermi level in the impurity band, and the activation energy of the thermally activated hopping between localized impurity states. For the x = 0.94 sample $d\rho/dT$ is positive at the lowest temperatures which suggests that the number of localized states is negligible but impurity band is still separated from the conduction band (nonzero ε_1). For the x = 0.85 sample only a metallic behaviour of $\rho(T)$ is observed indicating that in this latter case both these bands are no longer separated. Inset: R vs. $1/T$ at the lowest temperatures for the x = 1 sample. The solid line is a fit to the Mott's expression.

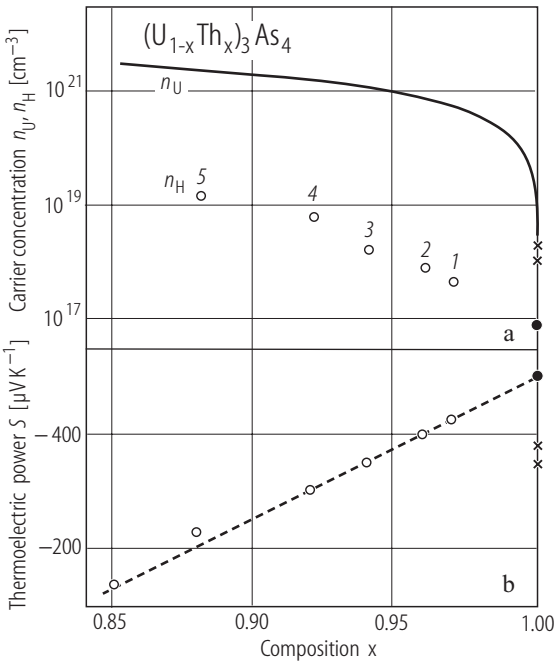

Fig. 178. $(U_{1-x}Th_x)_3As_4$. **(a)** Hall carrier concentration, n_H, and **(b)** thermoelectric power, S, vs. Th content, x, at T = 300 K [79MHW2]. Open circles are the experimental data found for different solid solutions (numbers correspond to the values of x specified in Fig. 179). Full circles denote the data obtained for the nominally pure Th_3As_4 sample, crosses mark the data got for two less pure Th_3As_4 samples. The solid line represents the concentration of U atoms, n_U, in the solid solutions. Note that n_U is about two orders of magnitude larger than n_H, even in the U-richest specimens. Dashed line marks a linear correlation between S and x (see also Fig. 179).

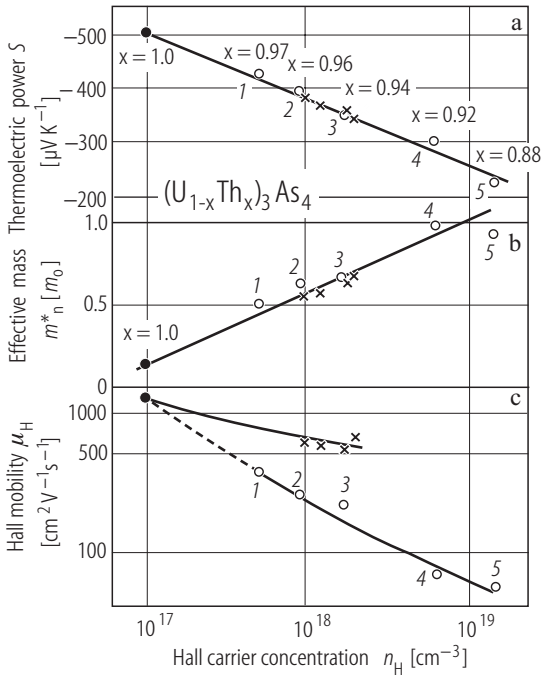

Fig. 179. $(U_{1-x}Th_x)_3As_4$. **(a)** Thermoelectric power, S, **(b)** electron effective mass, m_n^*/m_0, and **(c)** Hall carrier mobility, μ_H, vs. Hall carrier concentration, n_H, for samples 1-5 with x specified in panel **(a)** [79MHW2]. n_H as a function of x was determined as in Fig. 178. Open circles are the experimental data for the solid solutions. Full circles denote the results obtained for the nominally pure Th_3As_4 sample, crosses mark the data got for less pure Th_3As_4 samples. Note that both S and m_n^*/m_0, measured on different samples, obey the same dependence on n_H indicating similar shape of the conduction band. In contrast, μ_H behaves differently in Th_3As_4 with impurities and in solid solutions being lower in the latter one, most likely due to a stronger electron scattering.

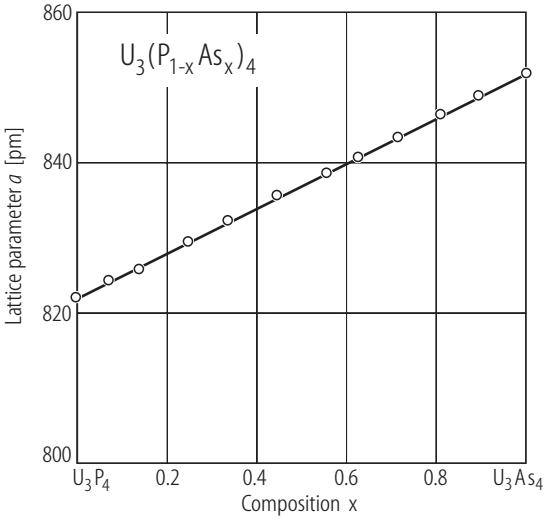

Fig. 180. $U_3(P_{1-x}As_x)_4$. Cubic lattice parameter, a, vs. As content, x [70TM]. The data follow Vegard's law.

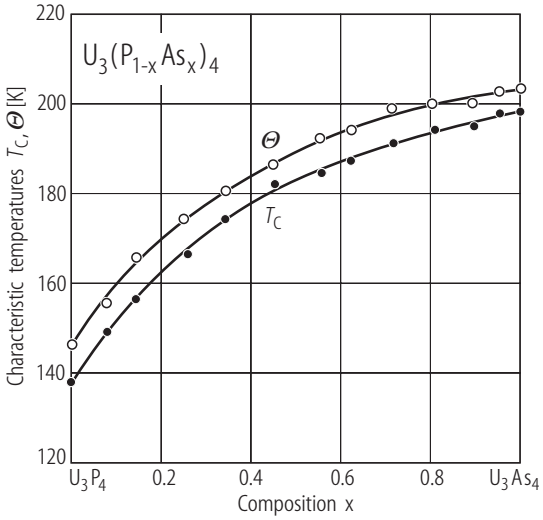

Fig. 181. $U_3(P_{1-x}As_x)_4$. Curie temperature, T_C, and paramagnetic Curie temperature, Θ, vs. arsenic content, x, as derived from magnetic susceptibility measurements in the range 90…500 K [70TM]. In the same temperature range the effective magnetic moments change with x in an almost linear fashion increasing from 2.79 μ_B for U_3P_4 to 2.96 μ_B for U_3As_4 (not shown).

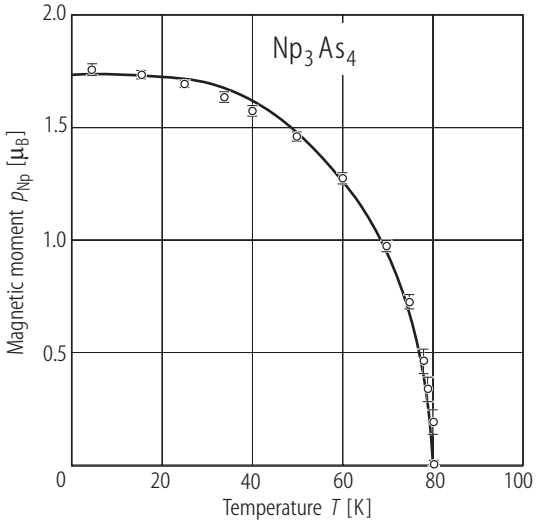

Fig. 183. Np_3As_4. Neptunium magnetic moment, p_{Np}, derived from the hyperfine field data (see Fig. 182b) vs. temperature, T, in the range 4.2…80 K [87ABFB]. The solid line is $p_{Np}(T)$ calculated in MFA within the refined CF model presented in Fig. 184 for α_1 = 0.61 and the ratio of scaling factors W/W_0 = 2.2, where W_0 is estimated from ab-initio calculations. Both the ordered moment and the ordering temperature are well reproduced.

For Fig. 182 see next page

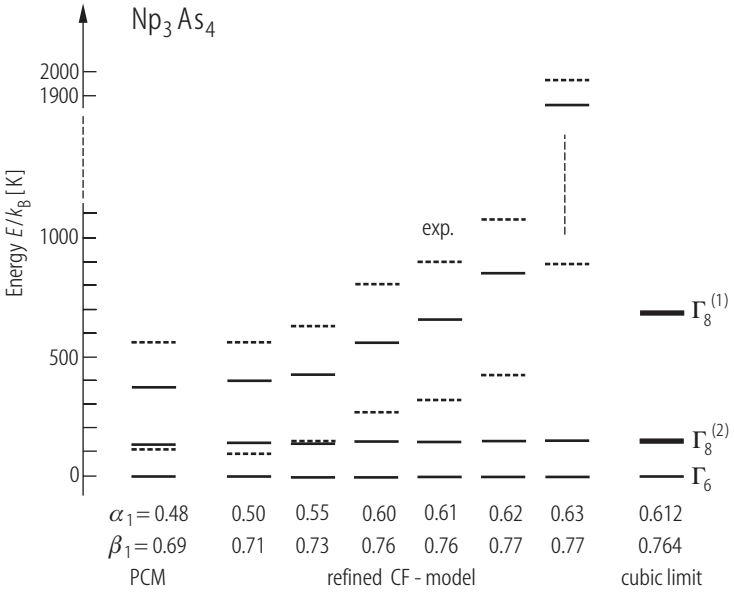

Fig. 184. Np_3As_4. Crystal field energy levels scheme calculated for Np^{4+} within three different approaches: 1) the Russell-Saunders coupling scheme and the nearest-neighbours approximation with the Sternheimer shielding factor σ_2 =0.8 (PCM); 2) the refined CF model for various compositions of the CF ground state; 3) the cubic limit [87ABFB]. For the details on the models and the relation between the coefficients α, β and γ, characterizing the ground state function, as well as for the discussion see the original paper. Full bars: Kramers doublets $|\psi_k\rangle = \alpha_k|\pm 9/2\rangle + \beta_k|\pm 1/2\rangle + \gamma_k|\mp 7/2\rangle$, k = 1,2,3; dashed bars: Kramers doublets: $|\phi_l\rangle = \delta_l|\pm 5/2\rangle + \varepsilon_l|\mp 3/2\rangle$, l = 4,5. The crystal field parameters used in the calculations are collected in Table T. See Fig. 183 for the comparison of the theoretical $p_{Np}(T)$ curve calculated within the refined CF model with the experimental results.

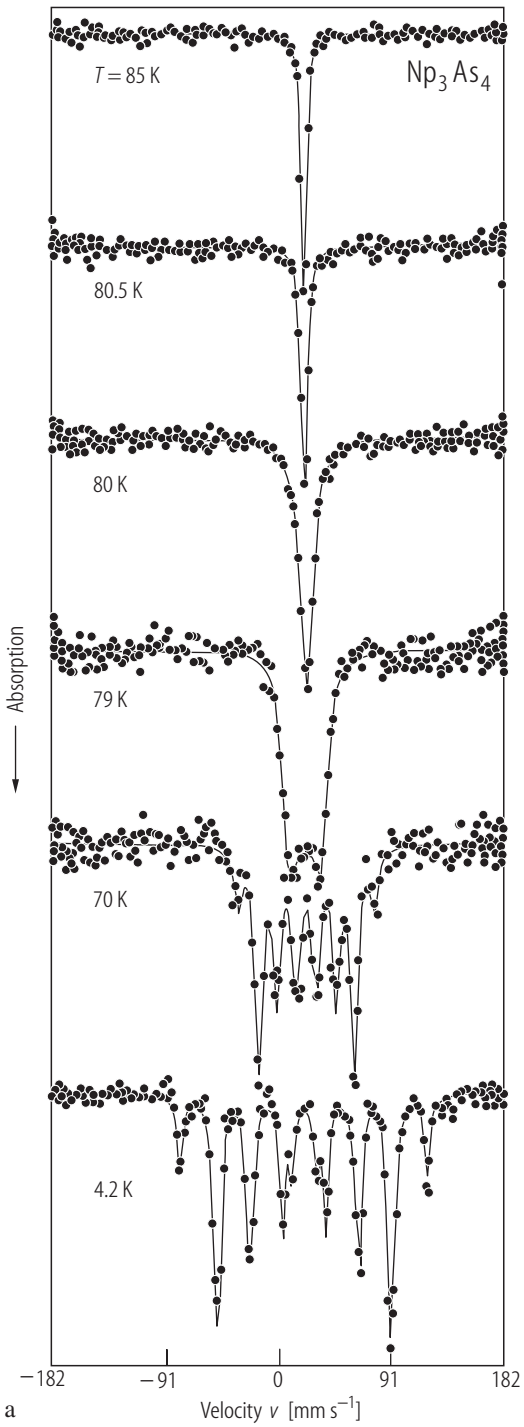

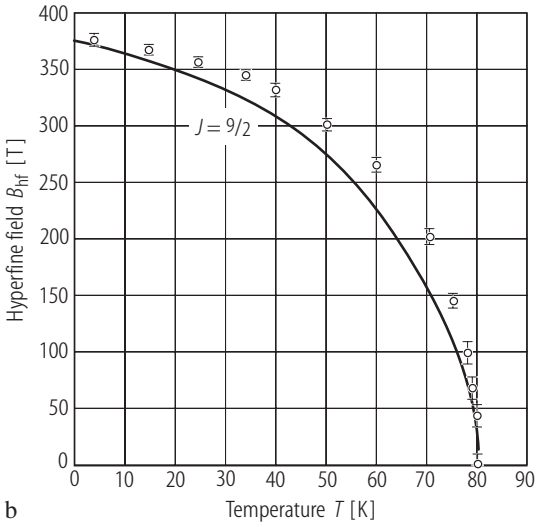

Fig. 182. Np_3As_4. **(a)** ^{237}Np Mössbauer spectra taken at various temperatures from 85 down to 4.2 K [87ABFB]. At 4.2 K the spectrum exhibits a magnetic splitting, which can be fitted to a single site. With increasing temperature the splitting diminishes and collapses into a single line near 80 K. All the spectra are symmetric without appreciable quadrupolar component (e^2qQ < 3 mm/s). The isomer shift with respect to $NpAl_2$ amounts to +5.9 mm/s, which implies tatravalent neptunium. **(b)** Hyperfine field, B_{hf}, vs. temperature, T, in the range 4.2…80 K [87ABFB]. The solid curve is the Brillouin function for J = 9/2, appropriate for a Np^{4+} free ion with the $^4I_{9/2}$ ground multiplet. Note the disagreement between the experimental data and the theoretical function. The hyperfine field at 4.2 K is 377 T, which corresponds to the ordered magnetic moment p_0 = 1.75 μ_B (according to the relation $\frac{B_{hf}}{p_{Np}} = 21.5\ T / \mu_B$). This value is much lower than the Np^{4+} free ion ordered moment of 3.2 μ_B. The reduction results from the crystal field effect (see Fig. 184).

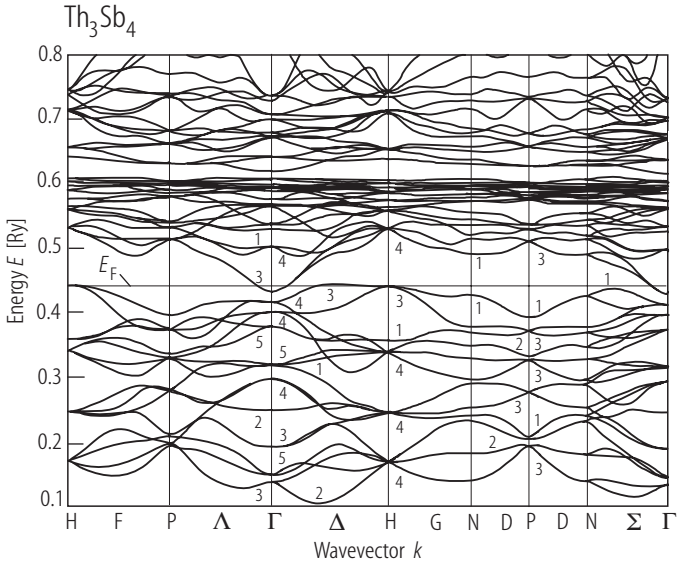

Fig. 185. Th_3Sb_4. Energy band structure calculated by the self-consistent APW method with LDA [90TKK]. For the details on the method used and comprehensive description of the results refer to the original paper. See also Fig. 186.

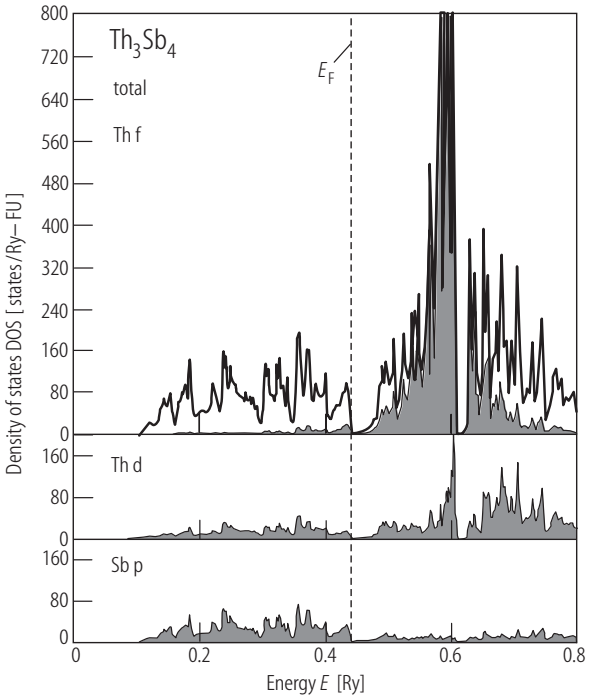

Fig. 186. Th_3Sb_4. Total and partial DOS calculated by the self-consistent APW method within LDA [90TKK]. The compound is a compensated semimetal. The valence band (derived from the Sb 5p states) and the conduction band (formed by the Th 6d states) slightly overlap yielding an equal number of electrons and holes. For further details see the original paper.

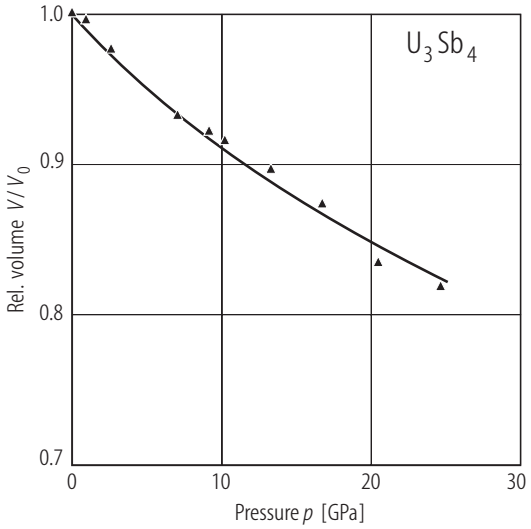

Fig. 187. U_3Sb_4. Relative volume, V/V_0, vs. pressure, p, up to 25 GPa [89SGBD]. The solid curve was calculated from the equation of state. The bulk modulus $B_0 = 86(3)$ GPa, and its pressure derivative $B_0' = 4.0$.

U_3Sb_4, U_3Bi_4

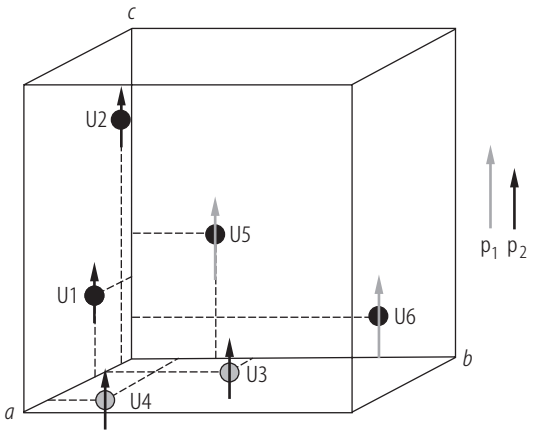

Fig. 188. U_3X_4, X = Sb, Bi. Magnetic structure [96GWH]. Shown are six uranium atoms distributed on six Bravais sublattices. The magnetic structure is considered to be collinear with a [001] easy axis and consists of two different types of U sites having different values of magnetic moment. At T = 8 K, the magnetic moments are 2.14(6) and 1.66(5) μ_B for U_3Sb_4 and 2.11(5) and 1.81(4) μ_B for U_3Bi_4. The difference between the magnetic moments on different U sites results from low local symmetry of the U ion environment. This collinear magnetic structure is however not possible in the case of S_4 symmetry [00KSK]. See Fig. 36 for a variant of noncollinear structure formed by two different magnetic moments, which correspond to two and four uranium atoms, respectively.

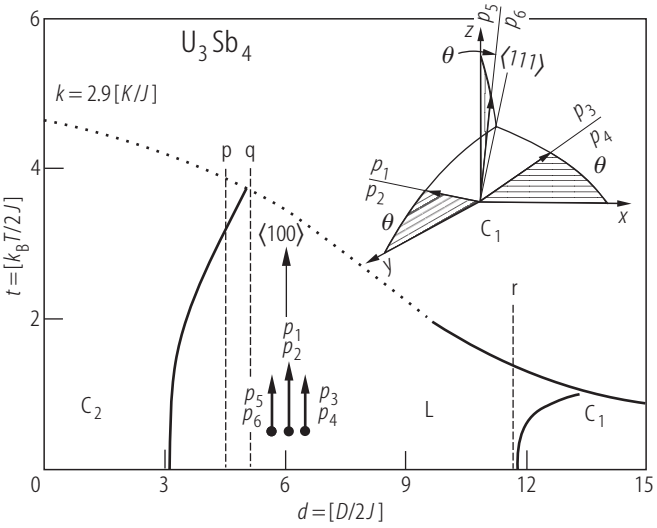

Fig. 189. U_3Sb_4. Part of the magnetic phase diagram in the (t,d)-plane, where $t = k_BT/2J$ and $d = D/2J$ [89MHFV]. The diagram was constructed for T = 0 K, and B = 0 in the framework of the S = 1 model and the mean field approximation (see also Fig. 40**)** and then applied to a multiaxial cubic ferromagnet at finite temperatures, as reported in [88O]. The exchange anisotropy constant was fixed at k = 2.9 [K/J], which is relevant for U_3Sb_4 (see [87HMOP]). The solid and dotted curves represent the first- and second-order phase transitions, respectively. The dashed vertical lines, labeled p, q and r, correspond to a value of 4.5, 5.1 and 11.7, respectively, for the parameter d. See the original paper for discussion of the magnetization behavior in these three cases. Inset: the arrangement of the magnetic moments in the C_1-type structure.

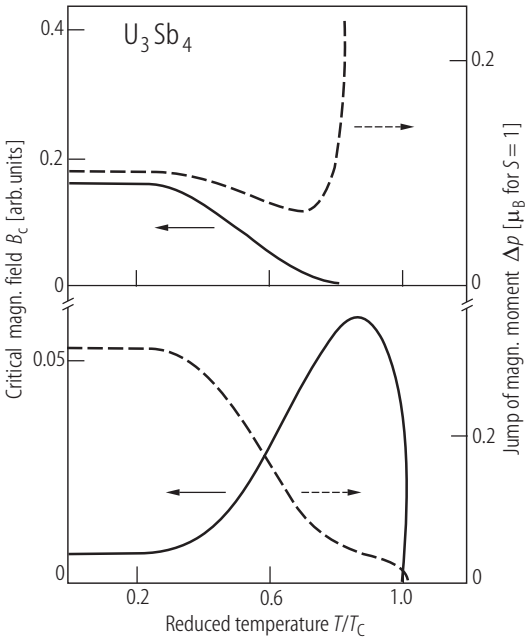

Fig. 190. U_3Sb_4. Magnetization jump, Δp (dashed curve, right-hand side scale), and critical field, B_c (solid curve, left-hand side scale), for the spin reorientation transition induced by magnetic field applied along the [111] axis, vs. reduced temperature, T/T_C, for case p (upper panel) and case r (lower panel) shown in Fig. 189 [89MHFV]. The case p is more relevant to the experimental temperature change of B_c while the case r is more relevant to the experimental temperature variation of Δp (see Fig. 191).

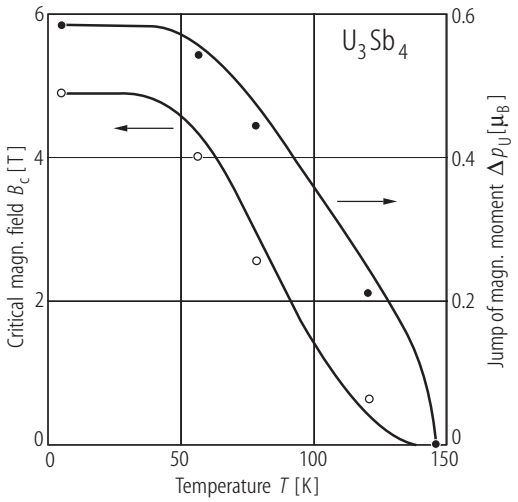

Fig. 191. U_3Sb_4, sc. Magnetization jump, Δp (full circles, right-hand side scale), and critical field, B_c (open circles, left-hand side scale), for the spin reorientation transition induced by magnetic field applied along the [111] axis, vs. temperature, T [89MHFV]. Δp and B_c were determined experimentally as shown in Fig. 194. The solid curves display the behaviour predicted theoretically within the model presented in Fig. 189 (case q). The values were adjusted to the experimental points at 4.2 K. Note a very good agreement between the calculated and measured data.

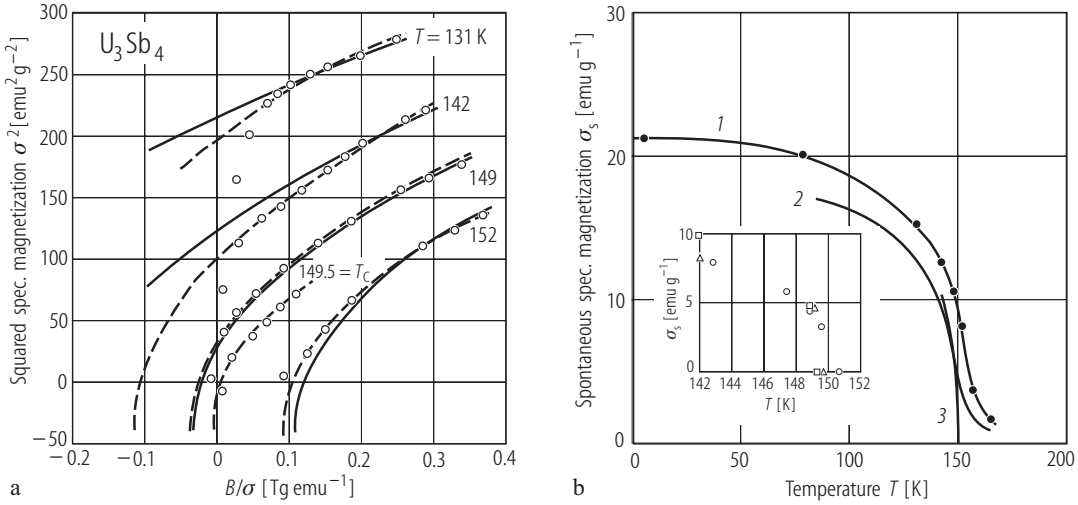

Fig. 192. U_3Sb_4. **(a)** Magnetization isotherms in the form of Arrott's plot σ^2 vs. B/σ [71SHMS]. The measurement temperatures are specified in the figure. The circles represent the experimental data; the solid and dashed curves are two different parabolical approximations (for description see the original paper). The two approximations coincide at T_C = 149.5 K, thus defining the ferromagnetic transition temperature. **(b)** Spontaneous magnetization, σ_s, vs. temperature, T, derived from *1* - the saturation moments (full circles) and *2* - taken from [64TSZ] (solid line) [71SHMS]. Curve *3* represents the dependence obtained by averaging the experimental values. Inset: $\sigma_s(T)$ around T_C obtained from the data presented in panel **(a)**. The squares and triangles correspond to the two approximations applied in panel **(a)**. The circles denote the results obtained by means of a linear approximation (not shown in panel **(a)**).

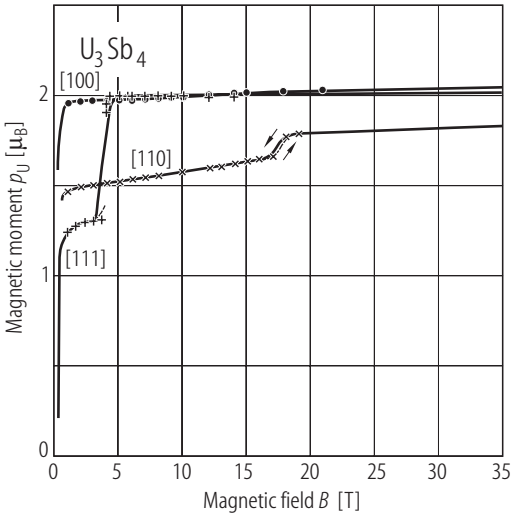

Fig. 193. U_3Sb_4, sc. Magnetic moment, p_U, vs. pseudostatic magnetic field, B, up to 35 T taken at T = 4.2 K along the [100], [110] and [111] axes [87HMOP]. Different symbols and lines represent the data obtained by different procedures of magnetization measurement in pulsed fields (for details see the original paper). The easy magnetic direction is the [100] axis. The jumps in p_U (B) occur for the [111] and [110] axes at 4.9 and 17.6 T, respectively. The uranium magnetic moment obtained by linear extrapolation to zero field of the high field data for the [100] and [111] axes is 2.00(1) μ_B. The spontaneous magnetic moment derived by the Arrott's method from the low-field data is 1.23, 1.46 and 1.98 μ_B for the [111], [110] and [100] axes, respectively. These values are close to those given by the cosinus law.

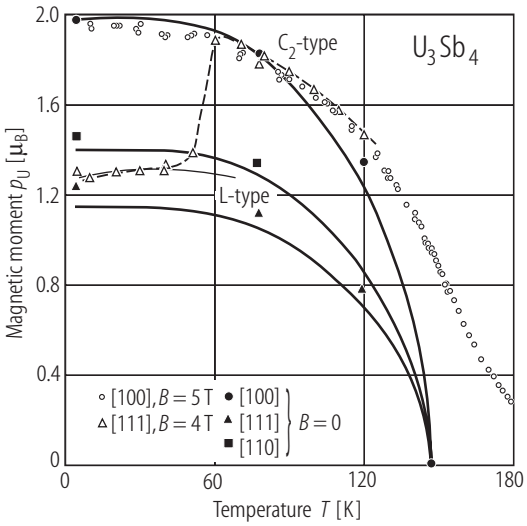

Fig. 195. U_3Sb_4, sc. Magnetic moment, p_U, vs. temperature, T in the range 4.2…180 K, measured along the [100] axis in a magnetic field of 5 T (dots) and along the [111] axis in a field of 4 T (open triangles) [89MHFV]. The full symbols denote the spontaneous magnetic moment, p_s, along the [100] (circles), [110] (squares) and [111] (triangles) axes. The bold solid curves are the calculated results (case q in Fig. 189) adjusted to the experimental data at 4.2 K for the spontaneous magnetization along the easy [100] axis. The thin solid curve together with the dashed curve emphasize the magnetization jump due to the change of the L-type magnetic structure to the C_2-type one (see Fig. 189).

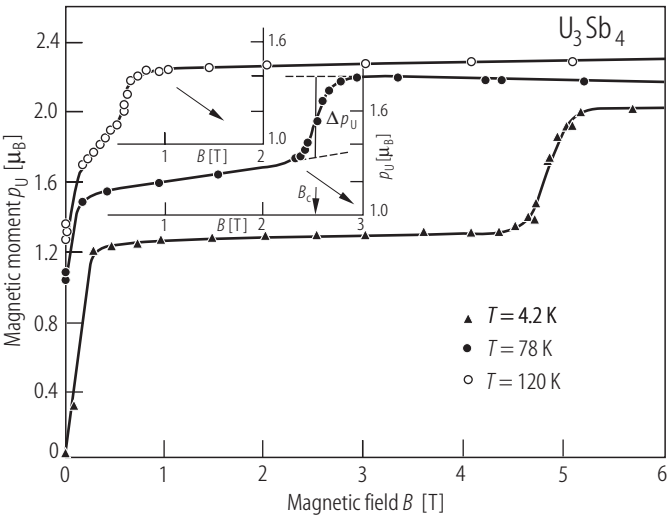

Fig. 194. U_3Sb_4, sc. Magnetic moment, p_U, vs. magnetic field, B, up to 6 T measured along the [111] axis at T = 4.2 K (full triangles), 78 K (full circles) and 120 K (open circles) [89MHFV]. Note different vertical scales. The solid lines serve as a guide for the eye, clearly visualizing the magnetization reorientation to the magnetic easy axis [100]. On the middle curve there is shown the determination of the critical field for the magnetization jump, B_c, and the magnitude of the jump, Δp_U, as the values at the midpoint of the spin-reorientation transition. With increasing temperature both B_c and Δp_U decrease (see Fig. 191).

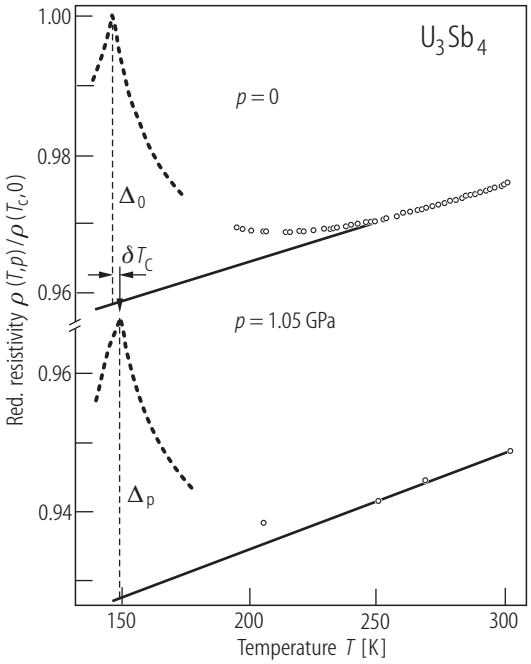

Fig. 196. U_3Sb_4, sc. Normalized electrical resistivity, $\rho(T,p)/\rho(T_C,0)$, vs. temperature, T, measured along the [100] axis in the vicinity of T_C and in the paramagnetic range at ambient pressure (upper curve) and at hydrostatic pressure p of 1.05 GPa (lower curve) [86HMD]. The solid lines mark a straight-line behavior of the resistivity at high temperatures and define the value of Δ_i (i = 0,p; dashed bars), which is a measure of the Fermi wave vector in ferromagnetic semimetals (see Fig. 46). The absolute value of the resistivity decreases with increasing pressure. At 300 K, $1/\rho(d\rho/dp)$ is –0.03 GPa^{-1}. The Curie temperature increases under pressure with the rate of 2.6 K/GPa. From the change of Δ_i under pressure the mutual shift of the conduction and valence bands was estimated to be of about 1.1 meV/GPa.

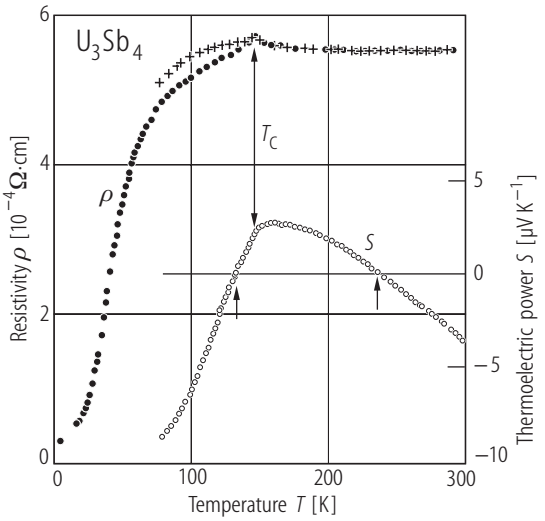

Fig. 197. U_3Sb_4, sc. Electrical resistivity, ρ (left-hand side scale), and thermoelectric power, S (right-hand side scale), vs. temperature, T [81HMK]. T_C = 147.2 K. Crosses and full circles represent the resistivity data for two different samples. A convex behaviour of $\rho(T)$ below T_C is ascribed to the domain effect. Note that $S(T)$ changes sign at two temperatures, i.e. at 133 and 236 K.

Fig. 198. U_3Sb_4. Normalized electrical resistivity, $\rho/\rho(T_C)$ (dashed lines, left-hand side scale), and thermoelectric power, S (solid lines, right-hand side scale), vs. temperature, T, measured in magnetic field of 0.85 T applied parallel and perpendicular to the direction of the current, i, or the gradient of temperature, ∇T [97WH]. Inset: schematic representation of the magnetic structure projected onto the [100] axis (for detailed description of the magnetic structure see Fig. 36). In the paramagnetic state the resistivity and the thermopower are isotropic, while in the ordered region the resistivity shows an anisotropic behaviour. The ratio $\rho(B \,||\, i)/\rho(B \perp i)$ reaches its maximum value of 2.46 at 81 K. The observed anisotropy is likely due to the spin polarization of the conduction bands. The thermopower is negative below 116 K and above 230 K, and positive between these temperatures. The ratio $S(B \,||\, i)/S(B \perp i)$ reaches its maximum value of 8.27 at T = 107 K, and shows a local maximum (= 2.56) at T = 127 K.

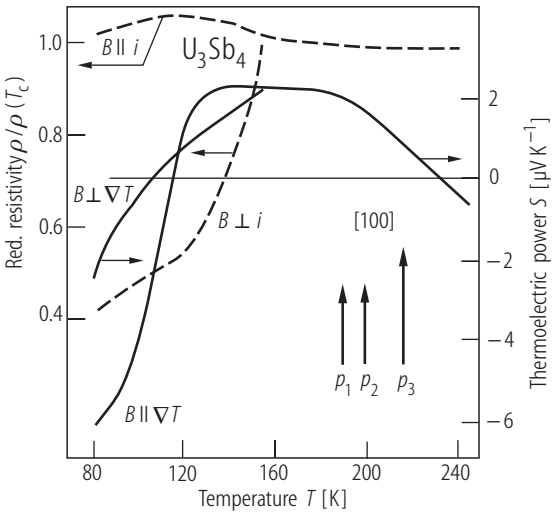

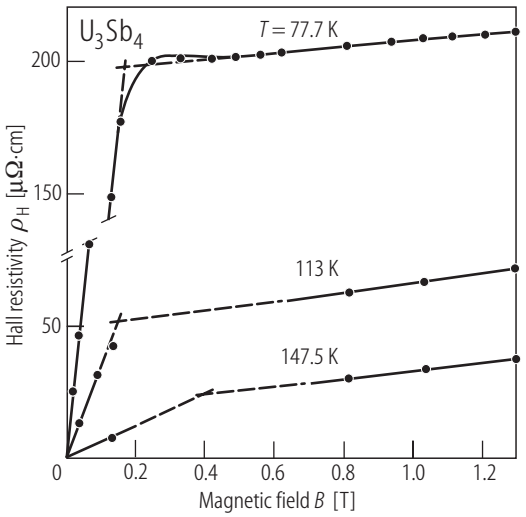

Fig. 199. U_3Sb_4, sc. Hall resistivity, ρ_H, vs. magnetic field, B, measured at T = 77.7, 113 and 147.5 K along the [110] axis with the electrical current flowing along the [112] axis and the field applied along the [111] axis [87HMOP]. The lines mark a straight-line behaviour of $\rho_H(B)$ in two field ranges. The Hall resistivity analyzed according to the formula $\rho_H = R_o B + R_S M$ where M is the magnetization, yields at T = 77.5 K the normal Hall coefficient $R_o = 5.0 \cdot 10^{-10}$ Ωcm/G and the spontaneous Hall coefficient $R_s = 6.3 \cdot 10^{-8}$ Ωcm/G. Note that R_o is positive, which suggests the dominance of hole conduction. Within a one-band model the hole concentration is $1.25 \cdot 10^{20}$ cm^{-3} i.e. 0.0079 hole per U atom. This value must be considered as an upper limit because U_3Sb_4 is considered as a semimetal having nearly equal number of holes and electrons.

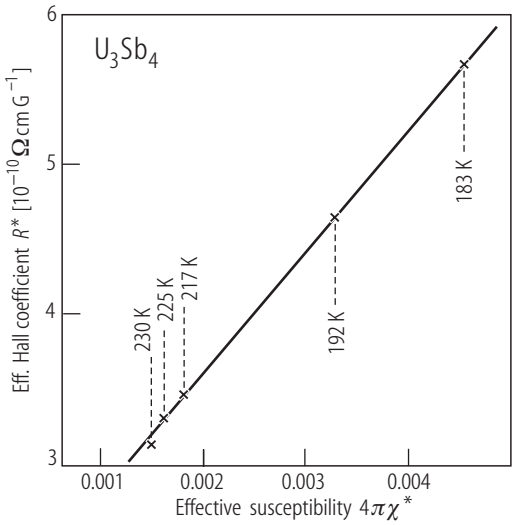

Fig. 200. U_3Sb_4, sc. Effective Hall constant, $R^* = \rho_H/B$, vs. effective susceptibility, $\chi^* = \chi/(1+4\pi\chi N)$, in the paramagnetic temperature range 183…230 K, measured on an unoriented crystal [87HMOP]. The susceptibility data were taken from [71TMS]. The solid line is the best fit yielding the coefficients $R_o = 2.7 \cdot 10^{-10}$ Ωcm/G and $R_s = 6.3 \cdot 10^{-8}$ Ωcm/G. Note that the value of R_s found in the paramagnetic range is the same as that derived in the ferromagnetic state (compare Fig. 199) but R_o is 45% lower, which suggests a change with the temperature in the free carrier concentrations and/or their mobilities.

For Fig. 201 see next page

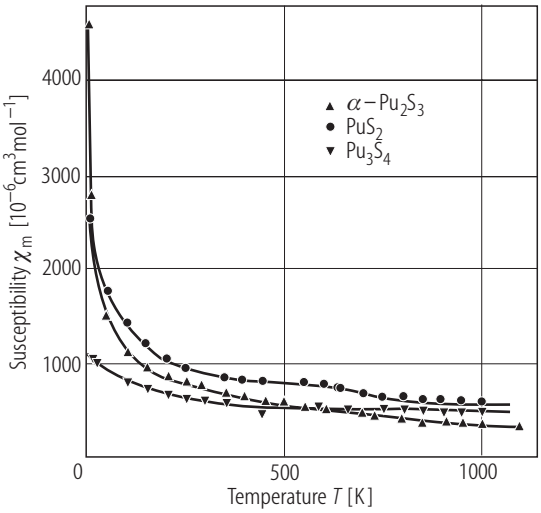

Fig. 202. Pu_3S_4, α-Pu_2S_3, PuS_2. Molar magnetic susceptibility, χ_m, vs. temperature, T, in the range 4…1200 K [69RD]. All three compounds are qualified to be antiferromagnetically ordered below T_N = 10, 7 and 15 K for Pu_3S_4, α-Pu_2S_3 and PuS_2, respectively.

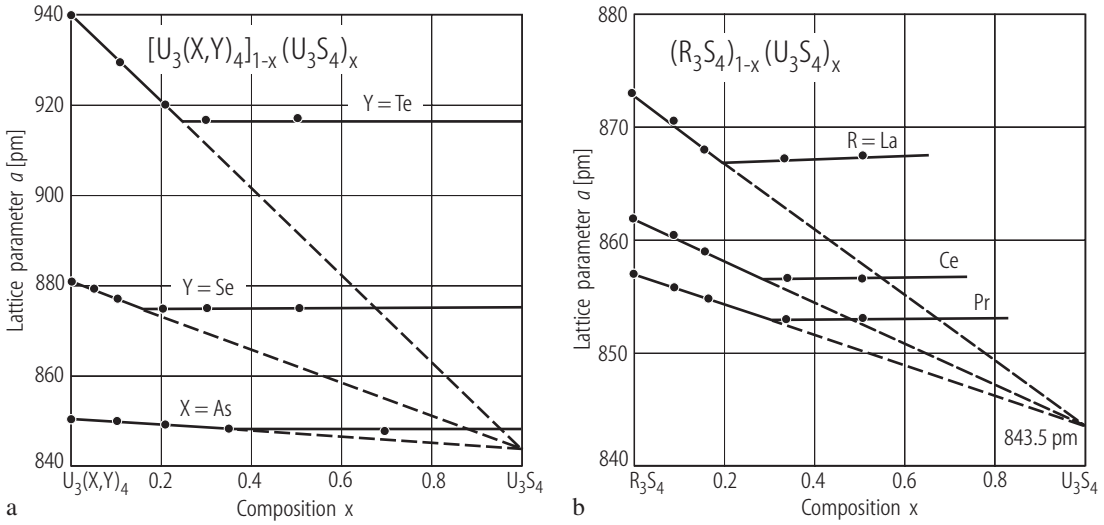

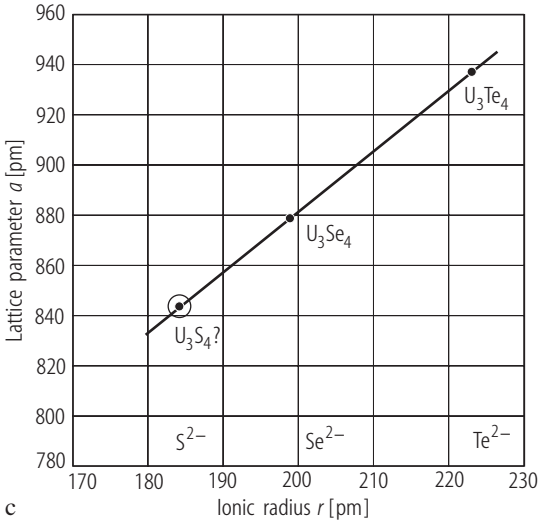

Fig. 201. U_3Y_4, Y = S, Se, Te. **(a)** Lattice parameter, *a*, vs. composition, x, for the solid solutions $U_3(Se;Te)_4$ and U_3As_4 with not existing "U_3S_4" [70DK]. Note the limits of such solid solutions where the highest content of "U_3S_4" solubility has been found for the arsenide. A hypothetical lattice parameter for "U_3S_4" is 840 pm. **(b)** Lattice parameter, *a*, vs. composition, x, for the solid solutions R_3S_4 (R = La, Ce, Pr) and not existing "U_3S_4" [70DK]. Note that the lattice parameter of the hypothetical "U_3S_4" is a little higher (843.5 pm) than that determined in panel **(a)**. **(c)** Lattice parameter, *a*, of U_3Se_4, U_3Te_4 and hypothetical "U_3S_4" vs. ionic radius, *r*, of S^{2-}, Se^{2-} and Te^{2-} [70DK].

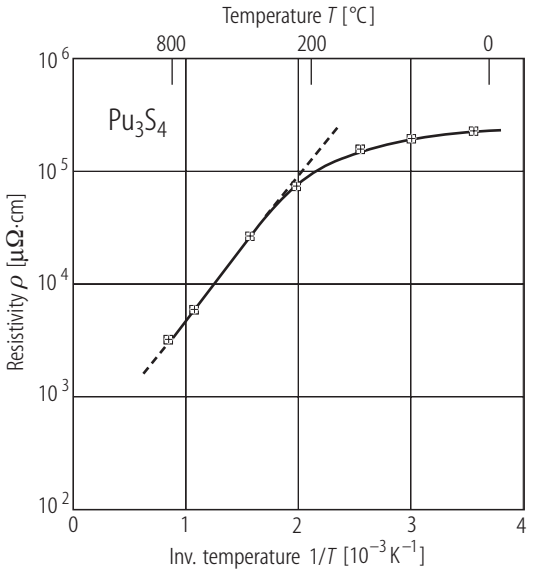

Fig. 203. Pu_3S_4. Electrical resistivity, ρ, vs. inverse temperature, $1/T$, in the range 300…1200 K [69M], cited by [69RD]. Note a semiconducting behaviour with the activation energy $E_g = 0.5$ eV.

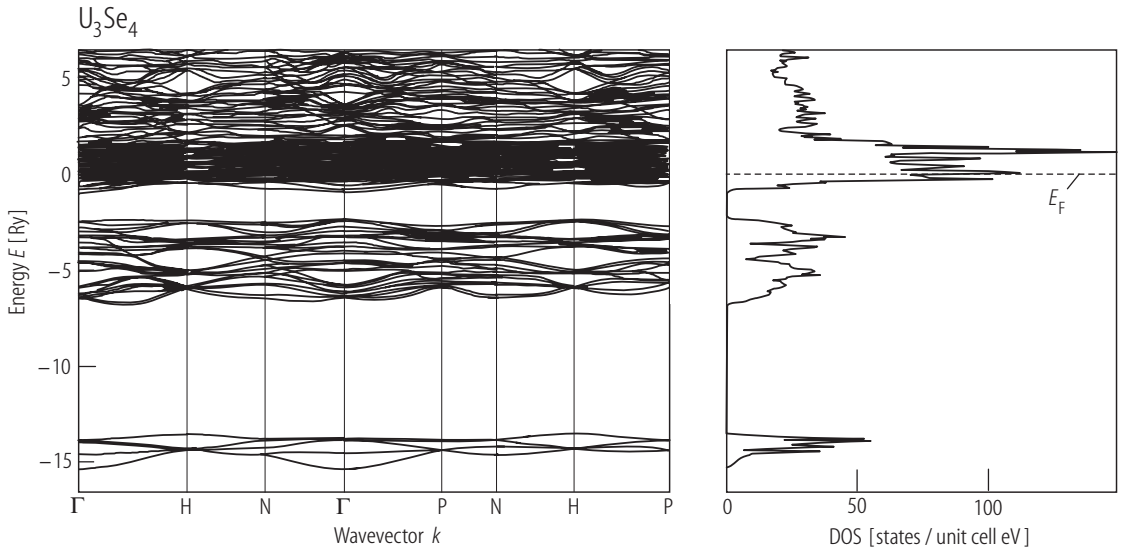

Fig. 204. U_3Se_4. Energy band structure and total DOS [in states/(unit cell eV)], calculated by fully relativistic, spin-polarized LMTO method using ASA with combined corrections included [99AHYP]. The LSDA calculations were based on the SDFT theory with von Barth – Hedin parametrization of the exchange potential. The Se 4p band is fully occupied and much below the Fermi level. Note that there is a large gap of about 1.3 eV between the p valence band and the U 5f band. The f-p mixing is clearly much less than that in the U_3X_4 pnictides and therefore the 5f electrons have a more localized nature.

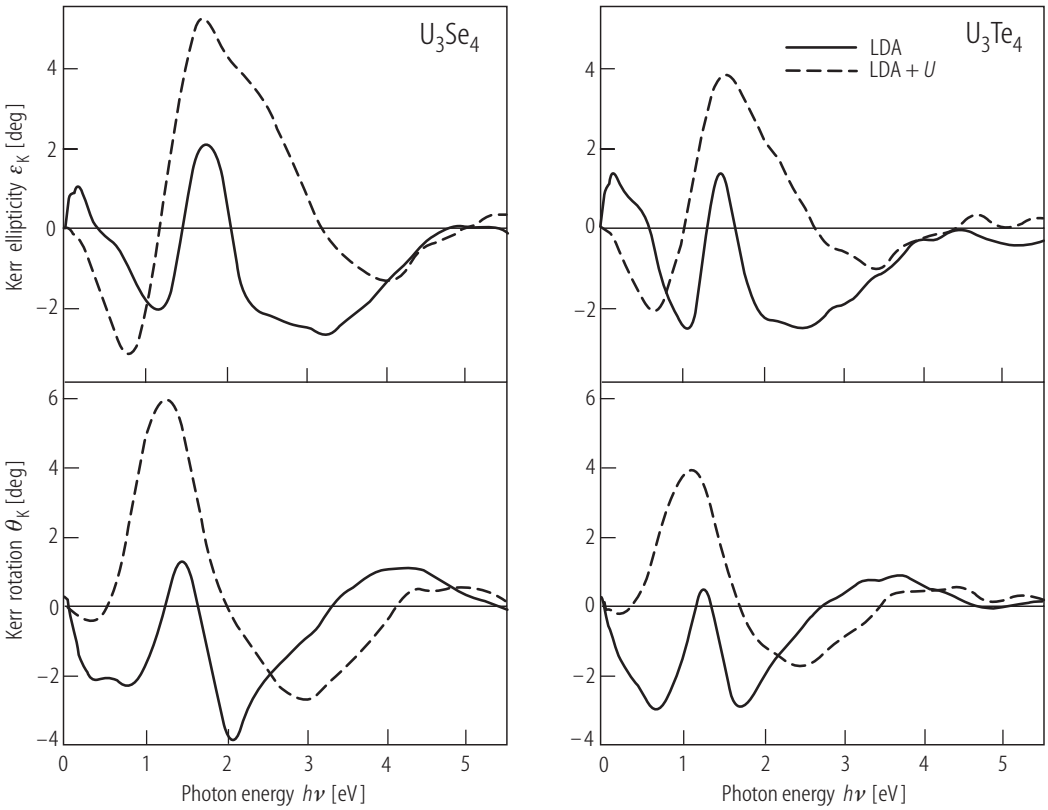

Fig. 206. U_3Y_4, Y = Se, Te. Kerr ellipticity, ε_K, and Kerr rotation, θ_K, vs. photon energy, $h\nu$, calculated ab initio by LSDA (solid curves) and LSDA+U (dashed curves) methods [99AHYP]. Note a large difference between the results of the two theoretical approaches. To date no optical and magnetooptical experimental data for the U_3Y_4 compounds are available.

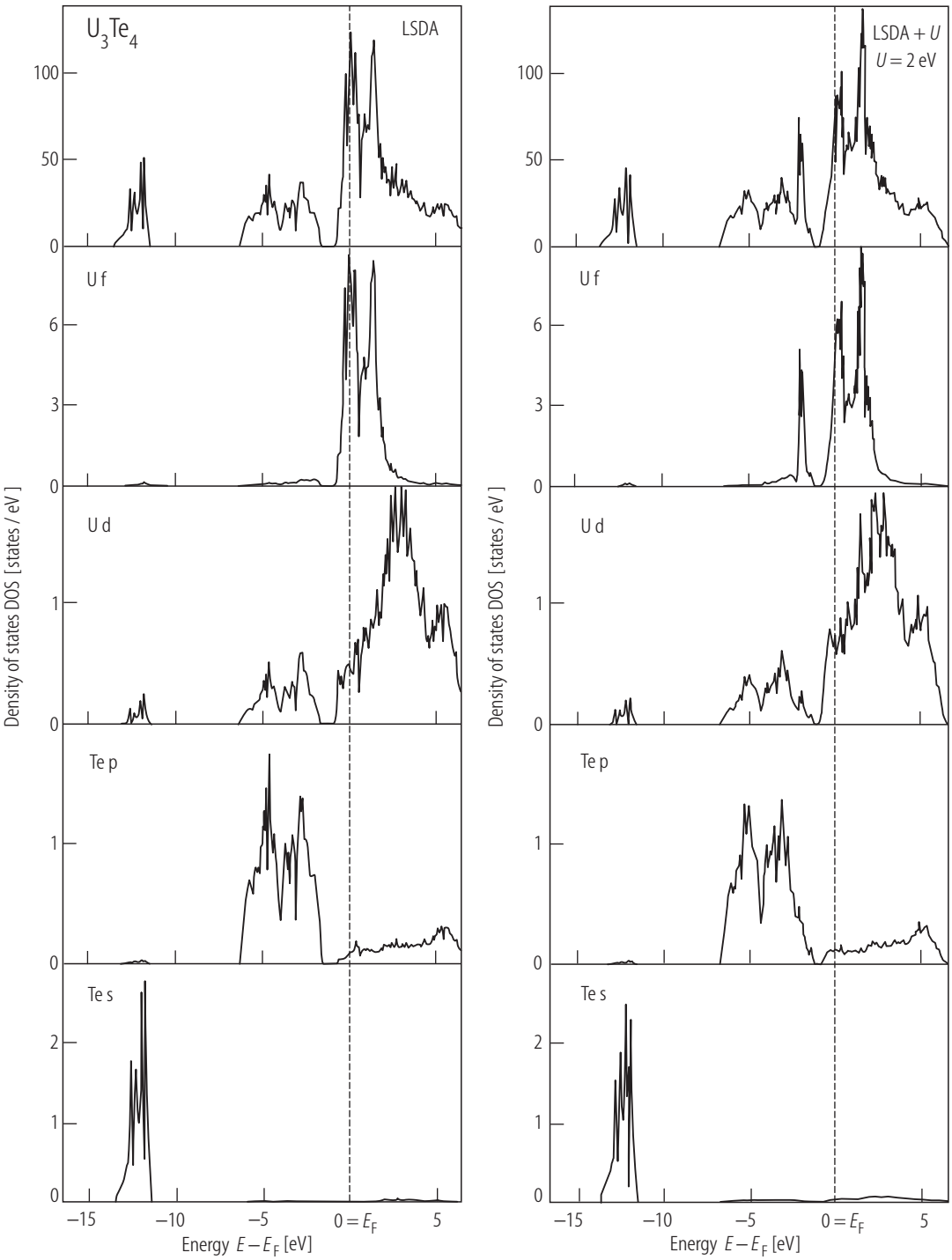

Fig. 205. U_3Te_4. Fully relativistic, spin-polarized total DOS [in states/(unit cell eV); top panel] and partial DOS [in states/(atom eV)], calculated using LSDA and LSDA+U (U = 2 eV) approaches [99AHYP]. For the U ions the $5f^2$ configuration was assumed. The gap between the Te 5p valence band and the U 5f band is 0.7 eV, i.e. it is smaller than that in U_3Se_4 (compare Fig. 204). This decrease is due to a larger extent of the atomic 5p orbitals as compared to the 4p orbitals, which results in broadening of the p valence band and its shift towards E_F.

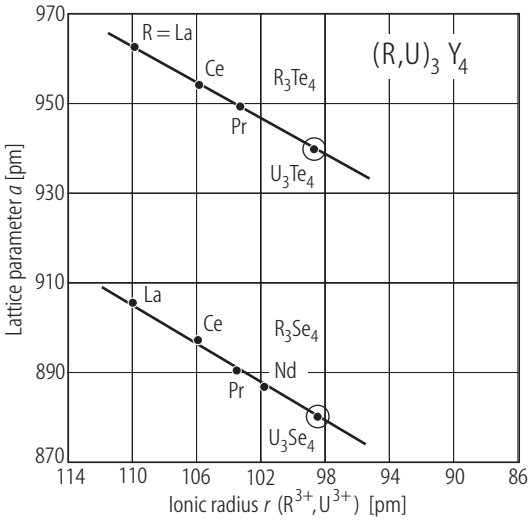

Fig. 207. $(R,U)_3Y_4$, R = La, Ce, Pr, Nd, Y = Se, Te. Lattice parameter, a, vs. ionic radius, r, of R^{3+} or U^{3+} [70DK]. Note that U_3Se_4 and U_3Te_4 follow well the lanthanide contraction (straight lines).

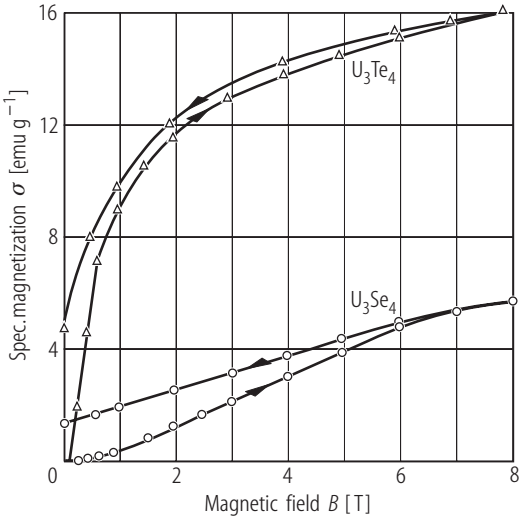

Fig. 208. U_3Y_4, Y = Se, Te. Specific magnetization, σ, vs. magnetic field, B, up to 8 T taken at T = 4.2 K with increasing and decreasing magnetic field (as shown by the arrows) [78T, on the basis of 72SMR]. Note a ferromagnetic like character of both compounds, however with no saturation in high magnetic fields.

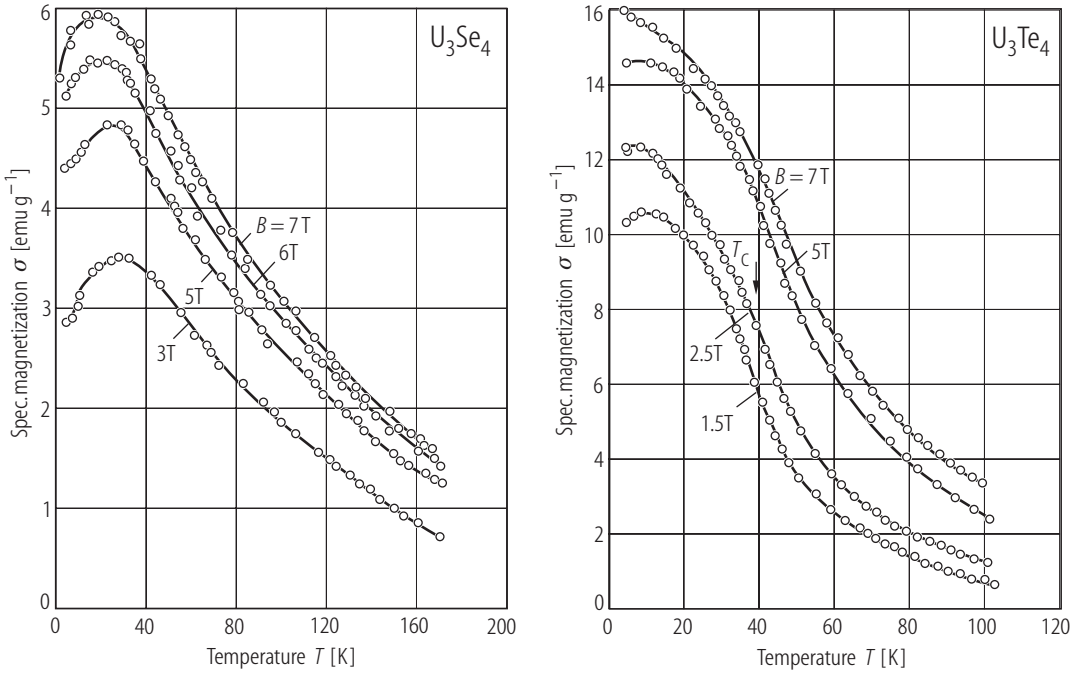

Fig. 209. U_3Y_4, Y = Se, Te. Specific magnetization, σ, vs. temperature, T, taken in several different magnetic fields, as indicated [72SMR]. $\sigma(T)$ of U_3Se_4 exhibits a maximum at about 35 K independent of the strength of magnetic field applied. For U_3Te_4 the arrow marks an inflection point at $T_C \approx 38$ K.

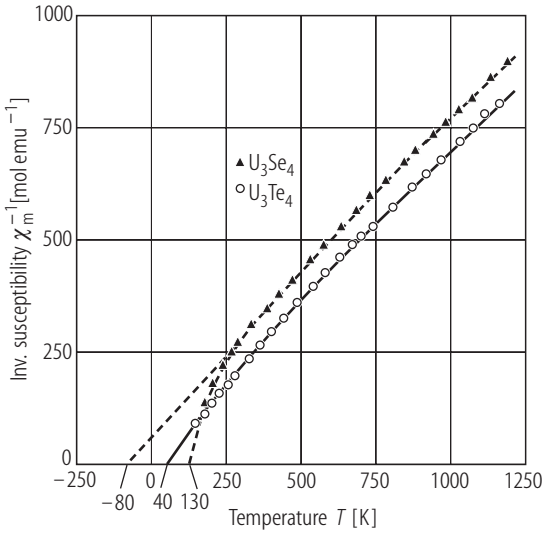

Fig. 210. U_3Y_4, Y = Se, Te. Inverse molar magnetic susceptibility, χ_m^{-1}, vs. temperature, T, up to 1200 K [71TMS]. For U_3Te_4 a Curie-Weiss behaviour of $\chi_m^{-1}(T)$ is observed in the range 130…400 K with the parameters given in Table F. The solid line is a fit of the experimental data obtained for U_3Te_4 to the formula $\chi_m^{-1} = \left(\frac{A}{T} + B\right)^{-1} - \lambda$ with the parameters listed in Table H. The dashed lines drawn for U_3Se_4 are only a guide to the eye showing that the Curie-Weiss law is followed.

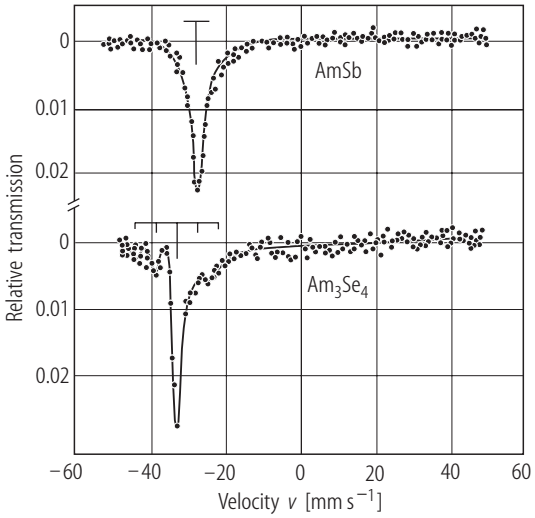

Fig. 211. Am_3Se_4. NGR spectrum taken at 4.2 K for the 59.6 keV nuclear gamma resonance in ^{237}Np compared to that of AmSb [71DLKS]. The solid line is a guide for the eye. No magnetic ordering is observed. The bar diagram denotes a quadrupole splitting. An asymmetric broadening of the quadrupole pattern results from the presence of paramagnetic relaxation of the Np ion in the nonmagnetic Am host. The coupling constant e^2qQ/h = 1870(100) MHz. IS = 27 mm/s (relative to a single line $NpAl_2$ absorber) indicating the trivalent state of Am ions.

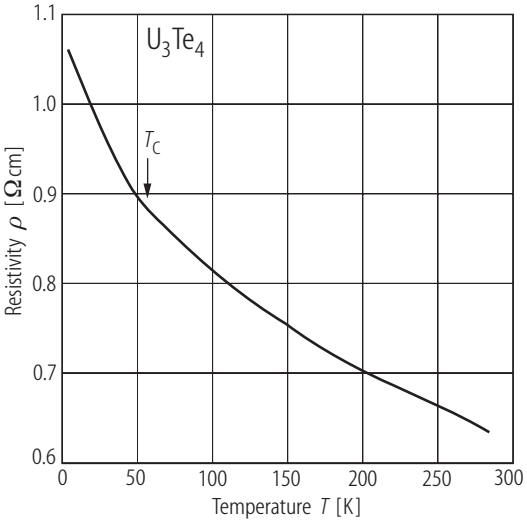

Fig. 212. U_3Te_4. Electrical resistivity, ρ, vs. temperature, T [81BJS]. The sample was obtained by arc melting pressed pellets containing pre-reacted stoichiometric 3:4 uranium telluride and subsequent very fast cooling down to room temperature. The change in the slope of $\rho(T)$ occurring at 50…60 K may be due to a transition to a ferromagnetic state. The observed increase in the resistivity with lowering the temperature is in agreement with the data reported by [63MMH].

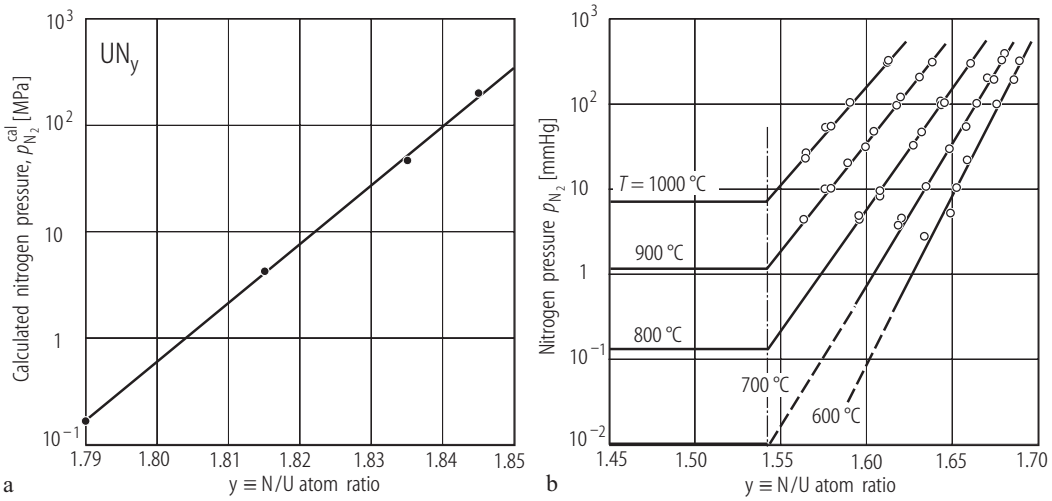

Fig. 213. α-U_2N_{3+x}. **(a)** Relation between pressure of nitrogen, p_{N_2}, and composition, y = N/U, at 300 ºC [95SFK]. The data were evaluated from the equation $a_N = p_{N_2}^{1/2}$, where a_N is nitrogen activity, which is the highest when using NH_3 in uranium nitride synthesis (see Fig. 452). **(b)** Equilibrium N_2 pressure, p_{N_2}, - temperature, T, - composition, y = N/U, relationship (p-T-C diagram) approached from U+N_2 (N-poor side as starting material, N/U ≤ 1.7) [71T2]. Note that the equilibrium N/U ratio is larger at lower temperatures and high p_{N_2} and that the slope of the isotherms is steeper when temperature is decreased. For example, the isotherms at 400 ºC (not shown) may be obtained only when the equilibrium is approached from the N-rich side (N/U ≥ 1.80) [93UTKM]. See the Introduction for the description of the higher uranium nitride synthesis. Other p-T-C diagrams were published by [64BB1], [64LH], [68MR], [73FT] (N-poor side) with less or more satisfactory agreement with [71T2] and by [98NNUK] at temperatures from 400 to 900 ºC (N-rich side). Based on these data free energies for the solution of N_2 in α-U_2N_{3+x} were obtained.

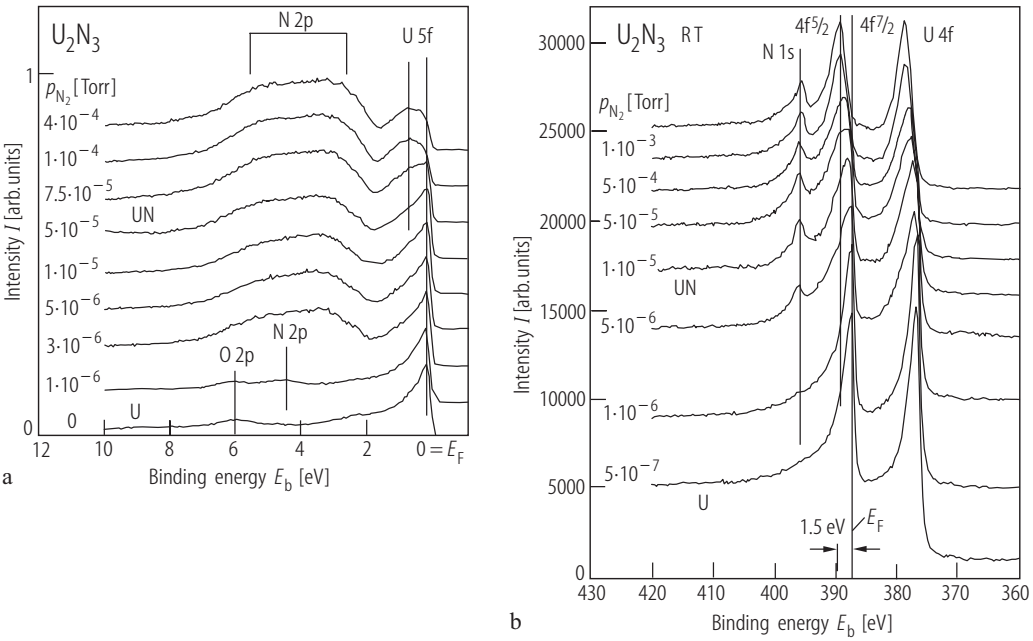

Fig. 214. α-U_2N_3, thin film. **(a)** Valence band spectra (HeII) at RT for systematic increase in partial pressure of N_2 [01BMGH]. Metallic uranium transforms first to UN and then to U_2N_3 at pressures above $5 \cdot 10^{-5}$ Torr. Note the gradual shift of the U 5f - band to higher binding energies and hence the decrease in DOS at E_F. **(b)** The $4f_J$ core level spectra for thin films deposited at RT with increasing N_2 partial pressure in the sputter gas [01BMGH]. After forming stoichiometric UN at $5 \cdot 10^{-6}$ Torr of N_2 pressure, the further increase of the N_2 partial pressure results in more symmetric $4f_J$ lines, which indicates an apparently lower DOS at E_F due to the formation of U_2N_3. Note that the binding energy shifts by 1.5 eV to higher energy.

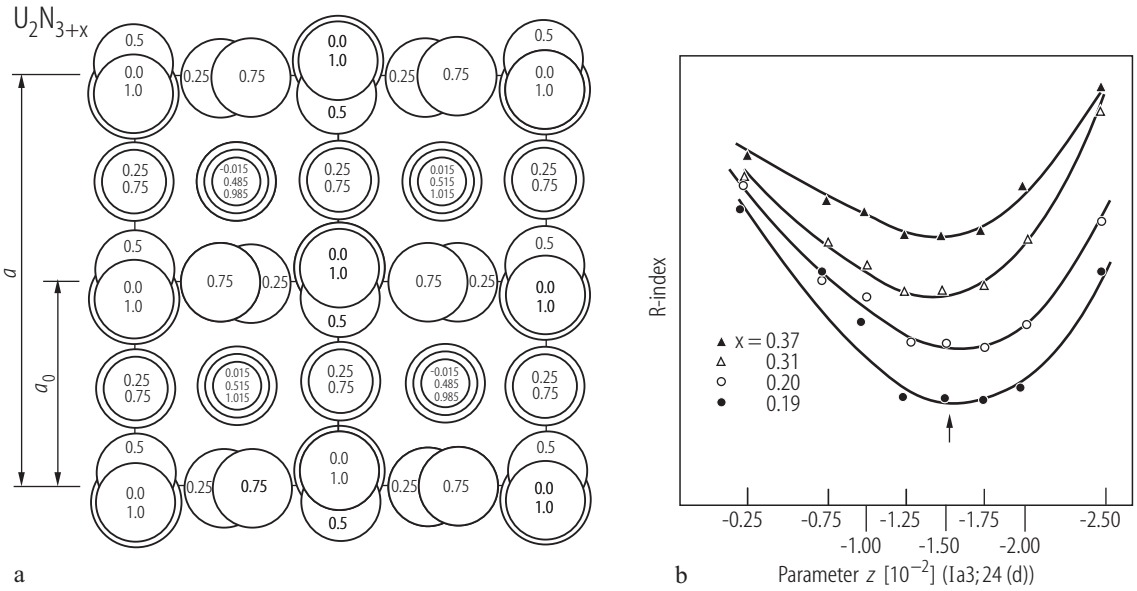

Fig. 215. α-U_2N_{3+x}. Uranium atom positions determined by X-ray diffraction for $0.19 \le x \le 0.37$ [73MTT]. Space group Ia3, Mn_2O_3-type structure, U(1): 8(b) (¼,¼,¼), U(2): 24(d) (*u*,0,¼). **(a)** Uranium atoms projected onto the (001) plane. Fractional *z*-coordinates are given. **(b)** The minimum in R indexes determines the free parameter $u = -0.015$ for all the compositions studied, in fairly good agreement with the data of [67TH], which established *u* by neutron diffraction experiment as –0.021 for x = 0.10 and 0.48. On the contrary, the results of [94SFIM] based on the change in the U-U distance (see Fig. 219) have shown that the positions of uranium atoms vary continuously with nitrogen content.

For Fig. 216 see next page

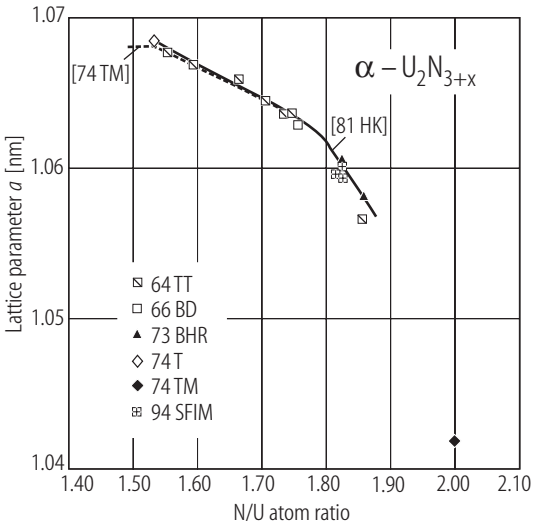

Fig. 217. α-U_2N_{3+x}. Lattice parameter, *a*, vs. N/U ratio [94SFIM]. For clarity some most deviated data have been omitted. The solid line yields the variation commonly accepted (see also [81HK]). The full diamond point corresponds to the hypothetical lattice parameter of 521 pm for stoichiometric UN_2.

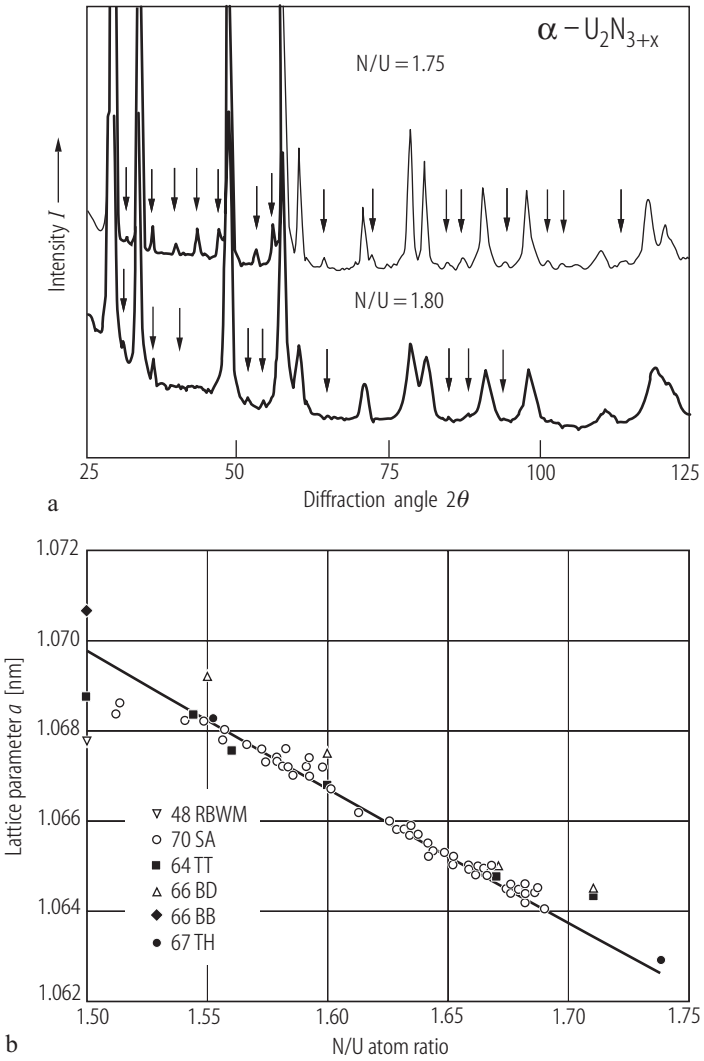

Fig. 216. α-U_2N_{3+x}. **(a)** X-ray diffraction patterns obtained for two samples with different N/U ratio: 1.75 (upper diagram) and 1.80 (lower diagram) [94SFIM]. The characteristic reflections of bixbyte type (bcc) lattice corresponding to the Mn_2O_3-type structure (see Fig. 221) are weak peaks marked by arrows. In contradiction to the earlier reports, also the nitrogen-rich phases (N/U > 1.80) have the bcc structure instead of the fcc CaF_2-type. It was claimed that beyond the N/U ratio of 1.75, the structure transforms from the bcc to the fcc-type [48RBWM, 64TT, 74TM]. **(b)** Pseudolinear variation of the lattice parameter, *a*, with the N/U ratio between 1.5 and 1.75 (open circles) [70SA]. For comparison the data by other authors are represented by different symbols, as indicated in the figure. There are added two *a*-values for $UN_{1.55(2)}$ and $UN_{1.74(3)}$ (full circles), taken from neutron diffraction study [67TH].

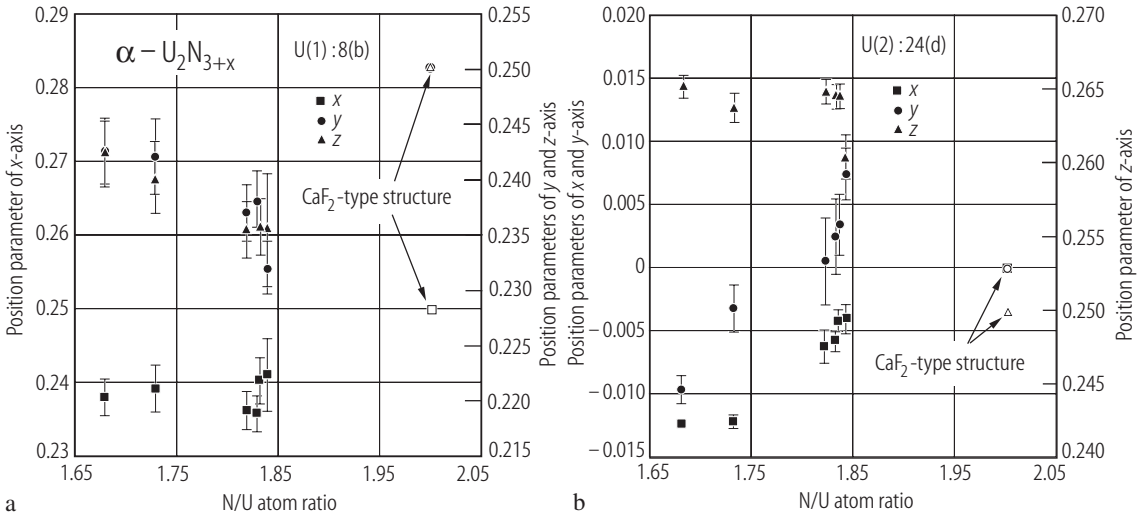

Fig. 218. α-U_2N_{3+x}. Positional parameters of **(a)** U(1) at 8(b) site and **(b)** U(2) at 24(d) site vs. N/U atomic ratio [94SFIM]. Note that in the lower N concentration (N/U < 1.75) the positional parameters do not change significantly but they vary rapidly for N/U > 1.75. The atoms U(1) and U(2) shift towards [0, $\bar{1}$, $\bar{1}$] and [1, 1, $\bar{1}$] directions, respectively. If the structure of α-U_2N_{3+x} would transform from bcc (Mn_2O_3-type) to fcc (CaF_2-type) the positional parameters should approach the values denoted by the open symbols.

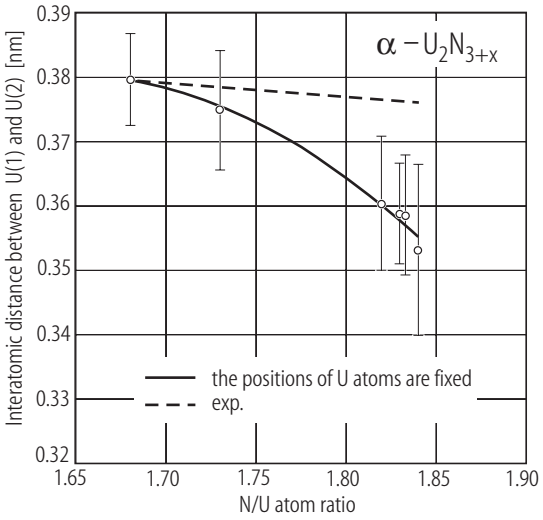

Fig. 219. α-U_2N_{3+x}. Uranium atoms distances, U(1)-U(2), vs. N/U atomic ratio, determined in neutron powder diffraction study [94SFIM]. The continuous decrease in U(1)-U(2) confirms the Mn_2O_3-type structure also for samples with the largest excess of nitrogen.

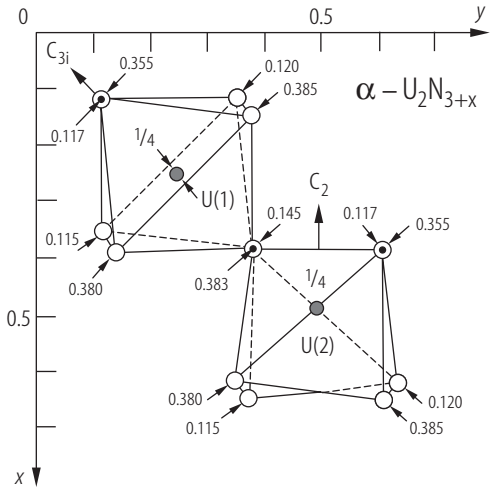

Fig. 220. α-U_2N_{3+x}. Nitrogen atom coordination around the uranium sites U(1) and U(2), projected on the *xy*-plane [75T]. In cubic α-U_2N_{3+x} there are 32 uranium atoms occupying the positions U(1) at 8(b) and U(2) at 24(d) sites and 48 + 16x nitrogen atoms occupying the positions N(1) at 48(e) and N(2) at 16(c). U(1) are fixed on the fcc sites with threefold inversion symmetry ($C_{3i} - S_6$), whereas U(2) are located in the sites with twofold symmetry (C_2) having in a simple case (see [94SFIM]) only one adjustable position u = –0.015 [67TH], –0.018 [73MTT], –0.019 [96BT]. For the U(1) sites the nitrogen atoms are situated in the corners of a very distorted cube, in which two atoms were removed from a face diagonal. All the U(1)-6N(1) distances are equal to 229 pm, and the U(1)-N(2) distances are 246 pm. U(2) atoms are slightly displaced from the center of the cube in the [100] direction. U(2) coordinates 2N(1) at the distance of 225 pm, 4N(1) at 234 pm and xN(2) at 238 pm. The positional parameters of U(2), N(1) and N(2) were taken from [67TH]. The low point symmetry of uranium atom sites probably causes the occurrence of a very complex magnetic structure of low dimensionality not being detected by neutron diffraction experiment at low temperatures [67TH].

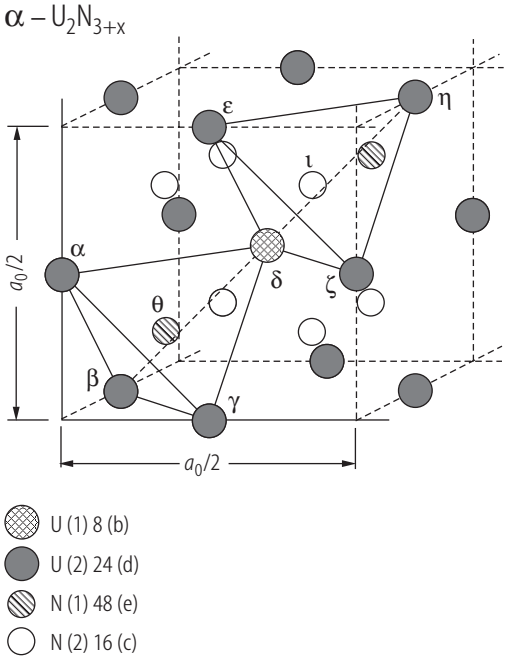

Fig. 221. α-U_2N_{3+x}. Crystal structure of the Mn_2O_3 type (space group Ia3) [94SFIM]. The excess nitrogen atoms N(2) fill the 16(c) position. The distances of the central atoms N(1) and N(2) to three U atoms at (γ,β,δ) and (ζ,η,δ), respectively, are the same, but the remaining distances to the fourth neigbouring U atom (α and ε) are slightly different, which causes the deviation of N atom positions from an ideal tetrahedral site.

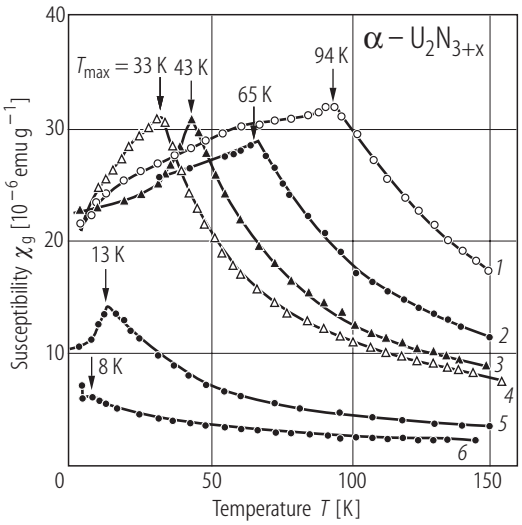

Fig. 222. α-U_2N_{3+x}. Mass magnetic susceptibility, χ_g, vs. temperature, T, for the samples with different N/U ratio: curve *1* - 1.55, *2* - 1.60, *3* - 1.64, *4* - 1.68, *5* - 1.75, *6* - 1.80 [75T]. The arrows mark possible antiferromagnetic phase transitions at T_{max} being however not confirmed by neutron diffraction experiments performed at 27 K [67TH] and at 4.2 K [96BT].

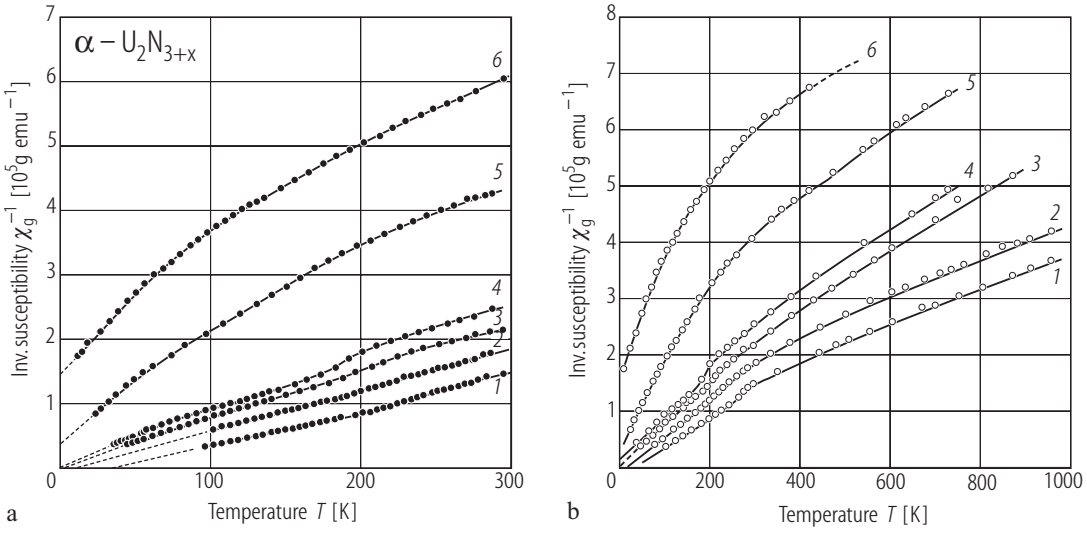

Fig. 223. α-U_2N_{3+x}. Inverse mass magnetic susceptibility, χ_g^{-1}, vs. temperature, T, up to **(a)** 300 K, and **(b)** 1000 K for the samples with different N/U ratio: *1* - 1.55, *2* - 1.60, *3* - 1.64, *4* - 1.68, *5* - 1.75, *6* - 1.80 [75T]. Inflections in the $\chi_g^{-1}(T)$ curves for the compositions with N/U below 1.70 arise due to the presence of uranium atoms on two different oxidation states (see Fig. 224).

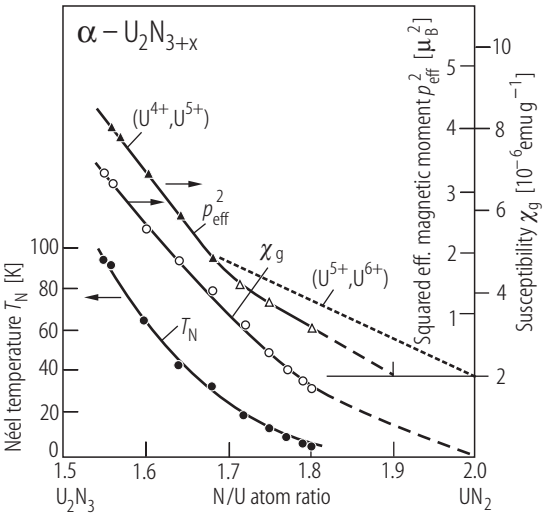

Fig. 224. α-U_2N_{3+x}. Squared effective magnetic moment, p_{eff}^2, mass magnetic susceptibility, χ_g, (right-hand side scales) and characteristic temperature T_{max} (left-hand side scale) considered as T_N (see Fig. 222) vs. N/U ratio [75T]. The fall of the susceptibility with increasing nitrogen content indicates a reduction in net magnetic moment. On this basis it was suggested that a progressive transformation of U^{4+} first to U^{5+} and then to U^{6+} takes place. Also the break in p_{eff}^2 as a function of composition, observed at N/U = 1.67, may be taken as a prove that uranium oxidation states (U^{4+}, U^{5+}) characteristic for lower compositions are probably changed into pure U^{5+} just at this composition. Then, with higher nitrogen content, the uranium oxidation state is gradually transformed into pure U^{6+} at UN_2 (the hypothetical ideal composition not obtainable even under high nitrogen pressure [64TT], [66BD], [73BHR]). On the other hand, the statistical model applied for analyzing the thermodynamic data of U_2N_{3+x} favors the $U^{4+}_{3/2}U^{6+}_{1/2}N^{3-}_3$ composition for x = 0 [73FT].

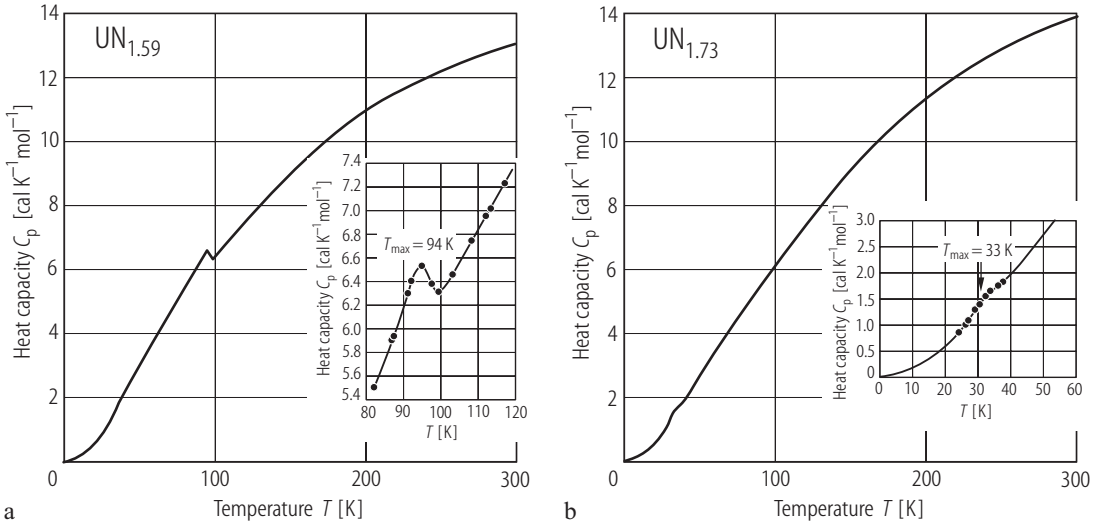

Fig. 225. α-U_2N_{3+x}. Heat capacity, C_p, vs. temperature, T, in the range 11…300 K for **(a)** $UN_{1.59}$ and **(b)** $UN_{1.73}$ [66CDM]. Insets: low temperature behaviour on enlarged scale. From the extrapolation to 0 K of the data described by the equation $C_p = \gamma T + \beta T^3$, the values $\gamma(0) = 50$ and 80 mJ/(mol K^2) were derived for $UN_{1.59}$ and $UN_{1.73}$, respectively. The obtained magnetic entropies of the transitions at 94 and 33 K are extremely small.

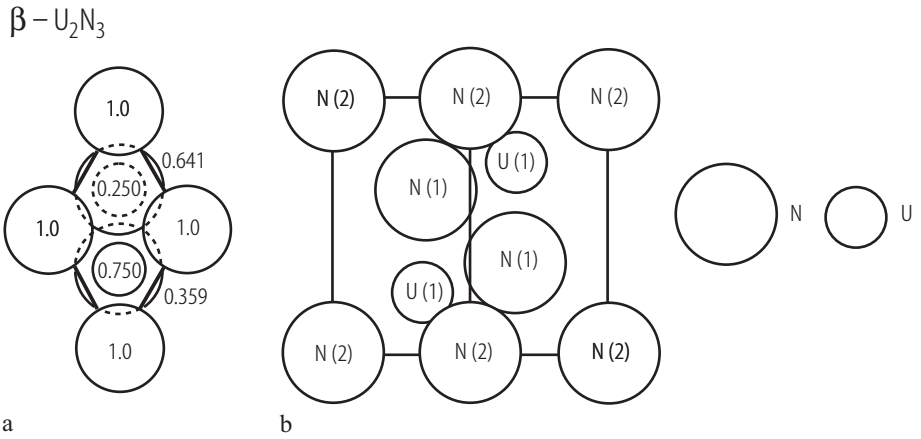

Fig. 226. β-U_2N_3. Crystal structure of the La_2O_3-type projected onto **(a)** the (001) plane and **(b)** the (110) plane [75MT]. The free parameters for U(1) at 2(d): z = 0.250 and N(1) at 2(d): z = 0.641 were found by neutron and X-ray diffraction. The uranium atom is surrounded by seven nitrogen atoms with various distances: 3 × [U(1) – N(2)] = 258.5 pm, 1 × [U(1) – N(1)] = 227.8 pm, 3 × [U(1) – N(1)] = 222.9 pm.

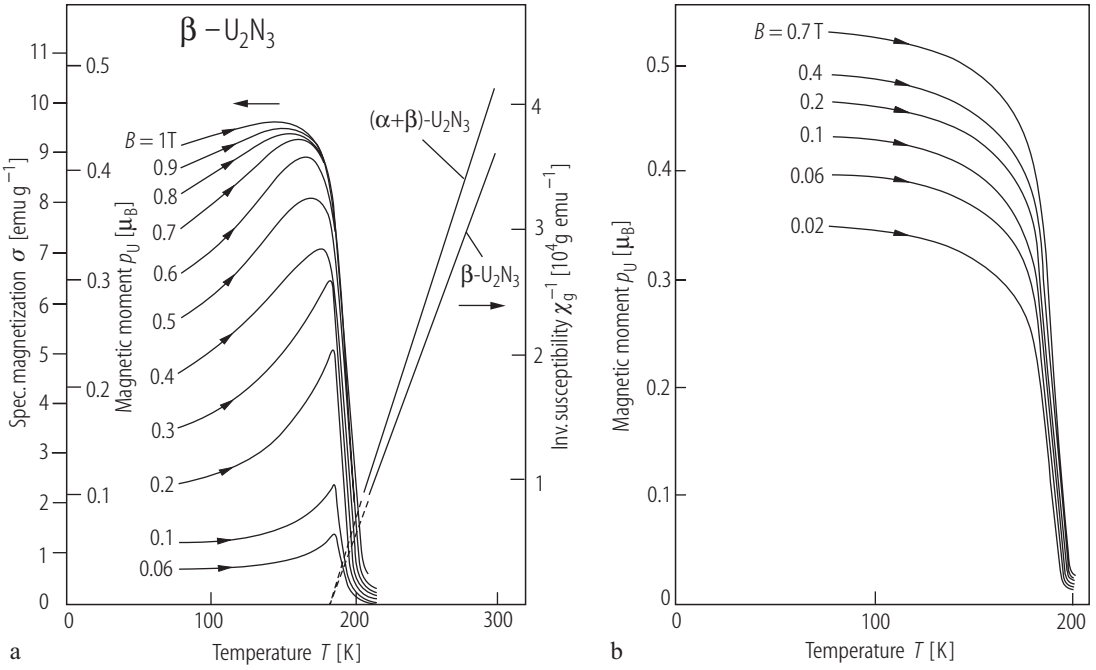

Fig. 227. β-U_2N_3. **(a)** ZFC magnetization (σ in emu/g and p_U in μ_B units), at various applied fields taken upon cooling the sample in zero field (left-hand side scale) and inverse mass magnetic susceptibility, χ_g^{-1}, (right-hand side scale) vs. temperature, T [72NTTK]. The measured sample contained 85% of β-U_2N_3. T_C = 182 K, p_{eff} corrected for pure β-U_2N_3 is 2.88 μ_B. See also [62TTL] and [82MT]. **(b)** FC magnetic moment, p_U, at various applied fields (indicated), taken upon cooling the sample down to 77 K [panel **(a)**] in an external magnetic field vs. T [72NTTK].